Available online at www.sciencedirect.com

ScienceDirect

Journal of Computational Physics 222 (2007) 504–535

JOURNAL OF COMPUTATIONAL PHYSICS

www.elsevier.com/locate/jcp

Multi-physics treatment in the vicinity of arbitrarily deformable gas–liquid interfaces

Petar Liovic, Djamel Lakehal *

Institute of Energy Technology, ETH Zurich, ETH Zentrum, 8092 Zurich, Switzerland

Received 20 July 2005; received in revised form 14 June 2006; accepted 28 July 2006

Abstract

A novel three-dimensional problem formulation is introduced for the simulation of turbulent interfacial multi-fluid flows. The strategy is built around the large eddy simulation (LES) concept, and can be employed for interfacial heat and mass transfer problems in which use can be made of either scalar transfer correlations, or exact mass/energy jump conditions. This multi-physics treatment capability at arbitrarily deformable interfaces translates into two main features: (i) a reconstructed distance function (RDF) is introduced to define a level-set interface-normal length scale, and (ii) an interfacial shear velocity is defined on the distance function support for further use in near-interface transport models. The solution algorithm uses VOF with piecewise planar interface reconstructions on a twice-as-fine mesh, and infers the convective mass fluxes from the interface solution to promote momentum conservation. The interfacial shear velocity defined on the distance function support is introduced to accommodate the asymptotic behaviour of turbulence approaching the interface in a proximity-dependent manner. Provided with highly accurate distance function data, the scheme generates near-interface damping functions that are second-order accurate and independent of interface orientation. The damping was found to be affected by errors introduced into shear velocity estimates by the high-frequency errors in the RDF scheme near the interface. The methodology has been applied for the simulation of a wave breaking scenario featuring multiple modes and interfacial length scales.

Keywords: Large eddy simulation; Deformable interfaces; Interface tracking; Incompressible flow; Navier–Stokes equations; VOF

1. Introduction

Realistic air–water flows featuring a wide range of interface length scales, such as wave breaking, will remain beyond the capability of DNS into the foreseeable future, but are increasingly becoming feasible for LES using the single-field representation of multi-fluid flows. The LES approach consists of directly solving flow scales larger than a typical characteristic length-scale of the dispersed phase; subgrid-scale (SGS) motions, including those resulting from the interaction between the phases, are statistically modelled. In

---

* Corresponding author. Also at ASCOMP GmbH, Zurich, Switzerland. Tel.: +41 1 6327073; fax: +41 1 6331662.
E-mail addresses: lakehal@ascomp.ch, lakehal@lsm.iet.mavt.ethz.ch (D. Lakehal).

0021-9991/$ - see front matter © 2006 Elsevier Inc. All rights reserved.
doi:10.1016/j.jcp.2006.07.030

large-scale interfacial flows, LES can be used to predict the flow physics down to the grid-resolved level. Supergrid turbulence scales should be resolved on both sides of the interface. The work initiated in our group (e.g. [1–3]) represents the first attempt to incorporate explicit SGS modelling for LES into an interface tracking-based, finite-volume code for the simulation of vigorous interface deformation and break-up.

In the case of wall-bounded flows, the usual Smagorinsky subgrid model alone is known to overestimate the SGS dissipation, and fails to predict the asymptotic behaviour of turbulence approaching the wall. A near-wall treatment such as using the van Driest damping function, or the dynamic modelling procedure of Germano et al. [4] are required to limit the over-dissipative behaviour of the model. The dynamic approach of Germano et al. does not readily extend to near-interface flows, because of the need to infer a specific direction for space averaging of the resolved-field-based length scale [5]. A strategy similar to near-wall damping should be applied for interfacial gas–liquid flows, where a strong shear occurs at the interface due to the density jump. A near-interface treatment that explicitly accounts for turbulence decay is therefore the most immediately promising means of ensuring that the small-scale effects are not exaggerated near the interface. Interface deformations at the grid scale being washed out by spurious subgrid eddy viscosity is one of the possible exaggerated near-interface effects that should be ameliorated.

Lakehal et al. [5] analyzed the DNS of the stratified gas–liquid flow over a sheared interface [6], and derived the first damping function for near-interface turbulence from the gas side. For low wave deformations, this correction allowed LES using the Smagorinsky kernel-based model in a pseudo-spectral code solver to generate relevant, less-dissipative turbulent statistics in an under-resolved (compared to DNS) stratified gas–liquid flow [5]. The main aim of the current work is to prescribe a new volume-of-fluid (VOF)-based scheme for coupling such explicit near-interface treatments into realistic flow scenarios featuring multiple fluid bodies and interfaces that deform, filament, fragment and coalesce in arbitrary ways.

As with the van Driest near-wall treatment used for the LES of boundary layers and channel flows, turbulence decay predicted by a near-interface damping function under low-*Re* number conditions should be distance dependent. Osher and Sethian [7] introduced the idea of level sets being advected by the flow, with the level quantity usually being a distance function. Level set methods in themselves are popular for interface advection, but are not universally embraced as the most effective for massively fragmented multi-fluid flows: front tracking [8,9] and volume-of-fluid methods [10–12] are also solid interface tracking foundations for such flows. VOF methods, in particular, are highly valued for their accuracy, robustness and local mass conservation properties.

The capacity to reproduce sharp fluid material properties across interfaces – density, molecular and turbulent viscosity in particular – is what makes VOF an excellent foundation for the proper use of LES for interfacial flows. This is because turbulence generation in sheared interfacial flows occurs at the interface, and strongly depends on how sharply the shear stress is captured there. A smeared interface is synonymous with weak interfacial shear, resulting in excessive dissipation of turbulent kinetic energy. Rudman [13] and Bussmann et al. [14] show the manner in which VOF solutions immediately couple into geometrically-reconstructed fluxes in momentum advection, to ensure rigorous conservation and stability in high-density-ratio flows (up to 10^{18}).

For the purpose of modelling near-interface flow physics using VOF for interface dynamics, a function for the distance to the interface is understandably required. The combined level-set/volume-of-fluid (CLSVOF) hybrid [15] is naturally attractive in this respect, provided VOF and level set advection results do not deviate, e.g. in massive topology changes (fragmentation). Cummins et al. [16] have recently demonstrated that the geometric foundations of VOF methods can be used to generate distance functions for interfacial transport models, and avoids having to address the issues introduced by choosing to advect distance functions using level-set methods.

In this work, we present a multi-fluid flow solution algorithm for 3D flows that uses volume tracking for interface motions, and uses a Smagorinsky SGS model for closure in LES incorporated within the single-fluid formalism. A novel, fully 3D scheme is introduced here for using data generated from the CVTNA VOF interface reconstruction scheme [17] to reconstruct the distance function throughout the flow domain. The scheme is complemented by a reconstructed interfacial shear velocity (RISV) algorithm, that in this work is active on the gas-side of the zero level of a reconstructed distance function (RDF). The implementation of the RDF and near-wall turbulence damping scheme based on RISV are described in detail. The schemes are validated using a range of test problems, prior to their application to real flow scenarios.

The strategy documented here is built around the LES concept, and incorporates heat and mass transfer capabilities treated either using scalar transfer correlations, or exact mass/energy jump conditions (i.e. solving scalar gradients on both sides of the discontinuity). Indeed, estimating the rate of heat/mass transfer ($\dot{m}$) across interfaces directly requires the scalar gradients to be carefully and accurately determined across the viscous interfacial sublayer, i.e. $\dot{m}h = \lambda_L \nabla T_L - \lambda_G \nabla T_G$, where h is the latent heat of phase change and λ the thermal conductivity. To account for inter-phase scalar transfer, one needs to incorporate adequate transfer laws in the mathematical model, independently from the flow regime. Incorporating such transfer laws should naturally be completed by resolving the region near the interface sufficiently well, such that heat and mass transfer could be directly determined. Achieving this is much more elusive, since for Prandtl and Schmidt numbers typical of applied situations, the thickness of the interfacial regions over which the scalar gradients are significant is a fraction of a millimeter. As such, resolution of these boundary layers is not possible at the scale at which interface tracking simulations could be performed. Well-established interphase heat/mass models, such as those based on surface renewal or surface divergence theories ([18,19]), require the determination of the interfacial shear (friction) velocity U_τ. In these models, the rate of scalar transfer K is determined by $K \equiv U_\tau (D/\tau)^m$, where $D = \nu/Pr$ is the molecular diffusivity of heat (or mass by replacing Pr by the Schmidt number Sc), τ a characteristic time scale, and m an exponent that depends on the nature of the surface in question (wall, sheared or free surface).

This paper is structured as follows: Section 2 introduces the physical modelling framework, namely the foundations of the LES concept extended for interfacial turbulent flows. Section 3 introduces the simulation tool, including an overview of algorithms and schemes, and the high-fidelity VOF, and VOF-augmented momentum advection. Section 4 explores the issue of subgrid-scale modelling further, in establishing modelling priorities and in the presentation of subgrid-scale models that better capture the asymptotic behaviour approaching interfaces. The reconstructed distance function and interfacial shear velocity algorithms required for the modelling of this near-interface physics are introduced in Section 5. The presentation of each of the above algorithms is supported by at least one validation test. Finally, Section 6 presents the application of the model to the wave breaking problem, where we discuss a selected set of comprehensive results.

2. One-fluid formalism

2.1. The primitive one-fluid equations

For flows consisting of immiscible fluid parcels of length scales larger than the grid size, phase inter-penetration is not presumed. Rather, jump conditions between the two phases are directly incorporated, such that the separate equations for each phase k can be replaced by a single set of equations describing the system. This is the starting point of the simplification from a multi-field to a single-field representation of the flow, in which the phases are identified locally using the indicator (or *color*) function C. In the continuous limit, color function C is the Heaviside function

$$C(\mathbf{x}, \mathbf{t}) = \begin{cases} 1 & \text{if } \mathbf{x} \text{ occupied by phase } k = G, \\ 0 & \text{if } \mathbf{x} \text{ occupied by phase } k = L \end{cases} \tag{1}$$

such that the C-weighted local density defined by

$$\rho \equiv \sum_k C^k \rho^k = C\rho^{\mathrm{G}} + (1 - C)\rho^{\mathrm{L}} \tag{2}$$

reduces to liquid density ρ^{L} or gas density ρ^{G}. The color function C helps describe the interface motion by the topology equation:

$$\frac{\partial C}{\partial t} + \mathbf{u}_j \frac{\partial C}{\partial x_j} = 0, \tag{3}$$

where the interface velocity $\mathbf{u}_j$ reduces to the local fluid velocity $\mathbf{u}$ in the absence of phase change.

Further, separate species mass conservation equations can then be described using the local density ρ:

$$\frac{\partial \rho}{\partial t} + \frac{\partial}{\partial x_j} \rho u_j = 0. \tag{4}$$

Since the fluids are taken to be incompressible, the density of a fluid particle is constant along its trajectory ($\mathrm{D}\rho/\mathrm{D}t = 0$). This suggests that the mass conservation of the system (4) can be represented by the combination of the continuity equation, $\partial u_j/\partial x_j = 0$, and the topology equation (3). This is valid as a statement of volume conservation in the single-fluid representation of multi-phase flows.

For momentum conservation, we propose a local viscosity μ that similarly takes the form of Eq. (2), i.e. $\mathrm{D}\mu/\mathrm{D}t = 0$. The constitutive relation between the rate-of-strain tensor S_{ij} and viscous stress tensor σ_{ij} presumes both fluid species to be Newtonian, i.e.

$$\sigma_{ij} = 2\mu S_{ij} \quad \text{with } S_{ij} = \frac{1}{2}\left(\frac{\partial u_i}{\partial x_j} + \frac{\partial u_j}{\partial x_i}\right). \tag{5}$$

The single-field momentum equations may thus be written as

$$\frac{\partial(\rho u_i)}{\partial t} + \frac{\partial(\rho u_i u_j)}{\partial x_j} = -\frac{\partial p}{\partial x_i} + \frac{\partial \sigma_{ij}}{\partial x_j} + \rho g_i + \gamma\kappa\hat{n}_i\delta. \tag{6}$$

The surface tension term here is $\gamma\kappa\hat{n}_i\delta$, where γ is the surface tension, κ is the interfacial curvature, $\hat{n}_i$ is the unit interface normal, and δ is the surface delta function. Finally, p denotes incompressible total pressure.

2.2. The filtered one-fluid equations

2.2.1. The component-weighted volume averaging (CWVA) procedure

The one-field equations (Eqs. (2)–(6)) are a micro-scale, primitive description of immiscible, incompressible, Newtonian two-phase flow. The macro-scale description (at the supergrid level) of the flow suggests all dependent variables contain subgrid-scale (SGS) components $f' = f - \bar{f}$, where the resolvable quantities $\bar{f}$ are obtained by convolution using a spatial filter G:

$$\bar{f}(x,t) \equiv G \otimes f = \int_D G(\mathbf{x} - \mathbf{x}')f(\mathbf{x}',t)\,\mathrm{d}\mathbf{x}', \tag{7}$$

verifying the normalization property

$$\int_D G(\mathbf{x} - \mathbf{x}')\,\mathrm{d}\mathbf{x}' = 1. \tag{8}$$

The filtered phase indicator function,

$$\overline{C}(x,t) \equiv G \otimes C = \int_D G(\mathbf{x} - \mathbf{x}')C(\mathbf{x}',t)\,\mathrm{d}\mathbf{x}', \tag{9}$$

is subsequently interpreted as a volume fraction indicator function, which is exact definition of the volume of fluid (VOF) quantity. The derivation of the filtered one-fluid equations presented here borrows essential features from the component-weighted volume averaging (CWVA) procedure employed in the context of the two-fluid formulation by Lakehal et al. [20]. In CWVA the flow quantities for each phase k were weighted in inter-penetrating-phase regions by the resolved volume fraction. In the single-field description of the flow, however, the coupling of $\overline{C}$ to the flow solution can instead be represented through the resolved density (Eq. (2)), which in essence is analogous to Favre averaging for compressible flows:

$$\tilde{f}(\mathbf{x},t) = \frac{\overline{\rho(\mathbf{x},t)f(\mathbf{x},t)}}{\overline{\rho(\mathbf{x},t)}}. \tag{10}$$

2.2.2. The filtered single-fluid conservation equations

Before proceeding further, it is perhaps useful to bring in the following conceptual clarification: In the single-fluid formalism for incompressible, isothermal multi-phase flows, the mass conservation of the system is described by both the continuity equation ($\partial u_j/\partial x_j = 0$) and the topology equation (3).

In using CWVA in this context, the property according to which filtering and differentiation commute can be extended to the multi-fluid flow context, too, provided the discretization is performed over uniform meshes. Applying relation (7) to the local density yields

$$\bar{\rho}(\mathbf{x},t) \equiv \sum_k \overline{C^k(\mathbf{x},t)\rho^k}. \tag{11}$$

Filtering the mass conservation equation (4) via relation (7) then performing CWVA (10) yields

$$\frac{\partial\bar{\rho}}{\partial t} + \frac{\partial}{\partial x_j}\bar{\rho}\tilde{u}_j = 0. \tag{12}$$

Equating next relation (11) into (12) allows the filtered topology equation to be written in the form:

$$\frac{\partial\overline{C}}{\partial t} + \frac{\partial}{\partial x_j}\overline{C}\tilde{u}_j = 0. \tag{13}$$

In both filtered equations above the commutation errors have been neglected. Note in particular that unlike their primitive formulations, these two expressions stand in a conservative form, very much similar to that holding for compressible flows.

Performing now the convolution product on the momentum equations and applying the resolved density-based CWVA (10) yields

$$\frac{\partial\bar{\rho}\tilde{u}_i}{\partial t} + \frac{\partial}{\partial x_j}(\overline{\rho}\tilde{u}_i\tilde{u}_j) = -\frac{\partial\overline{p}}{\partial x_i} + \frac{\partial\tilde{\sigma}_{ij}}{\partial x_j} + \overline{\rho}g_i + \gamma\overline{\kappa}\overline{\hat{n}}_i\delta \underbrace{-\frac{\partial\tau_{ij}}{\partial x_j}}_{\mathrm{I}} + \underbrace{\varepsilon_c^u}_{\mathrm{II}} + \underbrace{\varepsilon_d}_{\mathrm{III}} + \underbrace{\varepsilon_\gamma}_{\mathrm{IV}}, \tag{14}$$

where we have made use of the identity

$$\varepsilon_d \equiv \frac{\partial}{\partial x_j}[\bar{\sigma}_{ij} - \tilde{\sigma}_{ij}], \tag{15}$$

and introduced the local (phase-specific) SGS tensor, defined as

$$\tau_{ij} \equiv \bar{\rho}(\widetilde{u_i u_j} - \widetilde{u}_i\widetilde{u}_j). \tag{16}$$

Term II designates the sum of errors which appears if commuting between the filtering and differencing operators were not assumed explicitly. Term III represents the inter-phase net force between the two fluids at the subgrid level. It could represent the drag and lift forces of a bubble of a diameter smaller than the filter width. Similar to ε_d, the last term (IV) appears as a non-linearity error, which vanishes away from the interface, i.e.

$$\varepsilon_\gamma = \gamma\overline{\kappa\hat{n}_i}\delta - \gamma\overline{\kappa}\overline{\hat{n}}_i\delta. \tag{17}$$

It denotes the non-resolved counterpart of surface tension, that has been washed out by filtering.

3. Single-field flow solver for LES of multiphase flow

The MFVOF-3D code has been developed to be the vehicle for the tests and flow studies performed in this paper. MFVOF-3D is a finite-difference/finite-volume code for the simulation of transient high-density-ratio multi-fluid flows [21]. Within the staggered-grid single-field two-step projection flow solver, interfaces are tracked using a volume-of-fluid (VOF) method that is resolved on a *twice-as-fine* sub-mesh nested within the underlying solver mesh, as inspired by Rudman [13]. In the VOF scheme based on a 3D extension of the piecewise linear interface calculation (PLIC-VOF) concept, well-oriented piecewise planar reconstructions ensure interfaces remain compact over time, with the flotsam and jetsam associated with earlier VOF methods (e.g. [11,12]) suppressed. Surface tension is modelled using a fully kernel-based continuum surface force (CSF) method, and the linear equation system generated from the discretization of the pressure Poisson equation is solved using an efficient and robust multigrid-preconditioned GMRES solver.

3.1. Volume-of-fluid (VOF) interface tracking

The MFVOF-3D code features multiple novel and modern options for 3D PLIC-VOF, including the CVTNA and Youngs gradient interface reconstruction schemes, and the unsplit and direction-split advection algorithms. Centroid-vertex triangle-normal averaging (CVTNA) [17] is the first 3D interface reconstruction scheme that reliably achieves high-order accuracy within the confines of a 27-cell stencil. The Youngs gradient scheme [22] is formally less accurate than the second-order, planarity-preserving CVTNA, but is more efficient and can exhibit better low-resolution behaviour. The advantage of unsplit advection is in computational savings, in that it makes the relatively expensive CVTNA interface reconstruction scheme feasible by allowing it to be performed only once rather than three times. Note also that the combination of the Youngs gradient scheme for interface reconstruction with directional splitting can be particularly efficient. In the current work, the use of a twice-as-fine mesh allows the Youngs gradient scheme to match the performance of the CVTNA scheme on the equivalent unrefined mesh, while improving the tracking of high-curvature interfaces and reducing numerical surface tension effects associated with PLIC-VOF. For this reason, the Youngs gradient scheme is used as the default scheme. For future work featuring AMR and adaptive switching between CVTNA and the Youngs gradient in high-curvature areas only, we expect the general accuracy and efficiency promise of the CVTNA scheme to be fully realized.

3.2. VOF-augmented momentum advection

The MFVOF-3D code is based on a rigorous momentum-conservative formulation of the Navier–Stokes equations. A VOF-augmented advection scheme is used [13,14], in which local densities defining the convective fluxes are more accurately estimated by using material fluxes from the VOF scheme. This approach has the advantage of ensuring the bulk flow momentum discontinuity is reconstructed with the same sharpness as the VOF interface representation for the purpose of correctly capturing the jump conditions at the interface, while ensuring the transportiveness of advective fluxes and thus maintaining stability. When VOF is performed on the twice-as-fine mesh, volume-averaged local density estimates can be computed immediately, with no need for additional geometric operations. In the current method, the twice-as-fine VOF fluxes are used to augment advective fluxes in the van Leer scheme. The flow solver has proven to be extremely robust for high density-ratio, high-shear flows, and represents the foundation of the present LES code.

4. Subgrid-scale modelling

4.1. Importance of unresolved surface tension term closure

Full closure for all subgrid-scale terms in Eq. (14) is beyond the current state-of-the-art. Multiple research efforts are required to overcome the physics, mathematics and numerics issues associated with each SGS contribution, towards the outcome of reliable models. To motivate the modelling efforts presented in this paper, order-of-magnitude analysis is performed using *a priori* evaluation, in the spirit of the testing performed in [23]. The *a priori* evaluation here neglects consideration of term II and term III, by recalling the formalism's initial assumption of immiscible fluid parcels featuring length scales larger than the grid size, and assuming the use of regular meshes. The central issue in the current analysis relates to the unresolved surface tension term of Eq. (14) (term IV, Eq. (17)), and the order-of-magnitude of this term relative to the classical SGS stress term I that is ubiquitous across all LES of turbulent flow.

4.1.1. "Direct numerical simulation" of 2D bubble rise

The *a priori* test performed in the current order-of-magnitude analysis is 2D bubble rise. In this test, an air bubble of diameter 2 cm is initialized centrally in a 4 cm × 4 cm flow domain otherwise occupied by water. Using the MFVOF-3D code, a simulation of bubble rise is performed on a 200 × 200 × 1 mesh. The flow is laminar, or alternatively forced to turbulence by superimposing a fluctuating field, in which case the simulation is considered to be full DNS. From rest, the bubble is allowed to rise under buoyancy until T_1, at which time the simulation is stopped and an average shear velocity from the gas side of the interface (U_τ) is estimated (using the RISV scheme to be introduced later). The simulation then restarts with a white-noise perturbation imposed on top of the velocity field at T_1. The intensity of imposed turbulence is $\sqrt{u'^2} = \sqrt{v'^2} = \frac{2}{3}U_\tau$, representing a homogeneous isotropic turbulence. Time T_1 is chosen at a point in time at which large-scale laminar bubble deformation becomes apparent. Restarted turbulent simulations are continued from time T_1 to times T_2 and T_3, respectively. Time T_2 represents a point in time at which smaller-scale interface wrinkling away from the dominant 2D bubble deformation motion becomes noticeable, while time T_3 features more substantial interface wrinkling. In the current test given the geometry and initialization described, $T_1 = 0.025$ s, $U_\tau = 0.044$ m/s, $T_2 = 0.030$ s and $T_3 = 0.040$ s.

4.1.1.1. Filtering and term evaluation. With the DNS flow fields at times T_2 and T_3, filtering is performed to generate the subgrid-scale terms. For the u- and v-momentum equations, the comparisons of terms I and IV are $\epsilon_\gamma|_i$ versus $\partial\tau_{ij}/\partial x_j$.

The current *a priori* test involves filtering using the tophat filter with $\Delta = 2\sqrt{\delta x \delta y}$. CWVA using Eq. (10) and centered differencing are subsequently used to complete the generation of term I. For term IV, the "unfiltered" curvature is estimated using the height function approach as presented in [16,24], while the "unfiltered" normal is estimated using the CSF normal of Rudman [13] in the usual CSF normal approximation $\hat{\mathbf{n}}\delta \approx \mathbf{n} \approx \nabla C$ [24]. Tophat filtering for Eq. (17) subsequently completes term IV computation.

4.1.1.2. Spatial distributions. Fig. 1 shows the distributions of term I and term IV from the u-momentum equation; the results for the same terms from the v-momentum equation show little qualitative difference.

Initially concentrating on bulk SGS stress term I (row 1 of Fig. 1), the large magnitudes of the subgrid-scale terms I and IV in the immediate vicinity of the bubble interface are noteworthy. There is visible diminishing of bulk SGS stress levels in the absence of turbulence generation and under the stabilizing influence of the underlying large-scale 2D bubble rise motion. The increase in interfacial area and the volume of the high SGS stress region (as denoted by the red contour flooding) in the immediate vicinity of the interface from T_2 to T_3 counters the trend in the bulk flows away from the interface, and is accompanied by larger interface wrinkling. With no energy inputs into the flow from external sources, these trends suggest an out-scatter of energy from the large-scale bulk motions to the small-scale vortical structures that are cascading the interface length scale spectrum into the small scales – consistent with the LES findings in [2] for turbulent bubbling.

Fig. 1 presents two sets of unresolved surface tension results: the first for simulation results and post-processing normal estimates generated using a CSF kernel smoothing length $l_s = 2.5\sqrt{\delta x \delta y}$ (row 2), and the second using $l_s = 0.95\sqrt{\delta x \delta y}$ (row 3). The first smoothing length used is typical of standard CSF-based surface tension schemes, used to ensure an adequate amelioration of grid-based noise. The narrower second smoothing length localizes the surface tension estimate more to the vicinity of the interface, and pushes the limits on the smoothness properties of CSF estimates. Fig. 1 shows using $l_s = 0.95\sqrt{\delta x \delta y}$ brings the breadth of the interface support more into line with the breadth of the high-SGS-stress region at the bubble interface. Comparing the ratio of term IV to term I, it is apparent that, for the most part, unresolved surface tension term IV in the interface support is two orders of magnitude smaller than the turbulence SGS stress term I. The areas showing the unresolved surface tension to locally be larger than the SGS stress are on the fringes of the interface support, where the smeared-interface CSF computation of the interface normal is not overlapped by the more interface-localized distribution of high SGS stress levels. In terms of the large-medium-small-negligible classification of subgrid scale terms introduced in [23] and assuming SGS stress term I to be "large", we assert that unresolved surface tension term IV can be categorized as "small" for flow problems with relatively well-resolved interfaces.

4.1.2. Consequences for subgrid-scale term modelling

The 2D bubble rise flow features high SGS stress levels in the vicinity of the interface, as well as substantial gradients in the SGS stress moving from the interface into the bulk flow within the bubble. Given the great relative importance of the SGS stress term I in the vicinity of the interface, modelling of term I is the immediate priority in the current work. The potentially high intensity of turbulence cascading down to smaller interface wrinkling scales demands particular attention, with the specific intention of ensuring the imposition of physically correct asymptotic behaviour of turbulence approaching interfaces. The sporadically significant

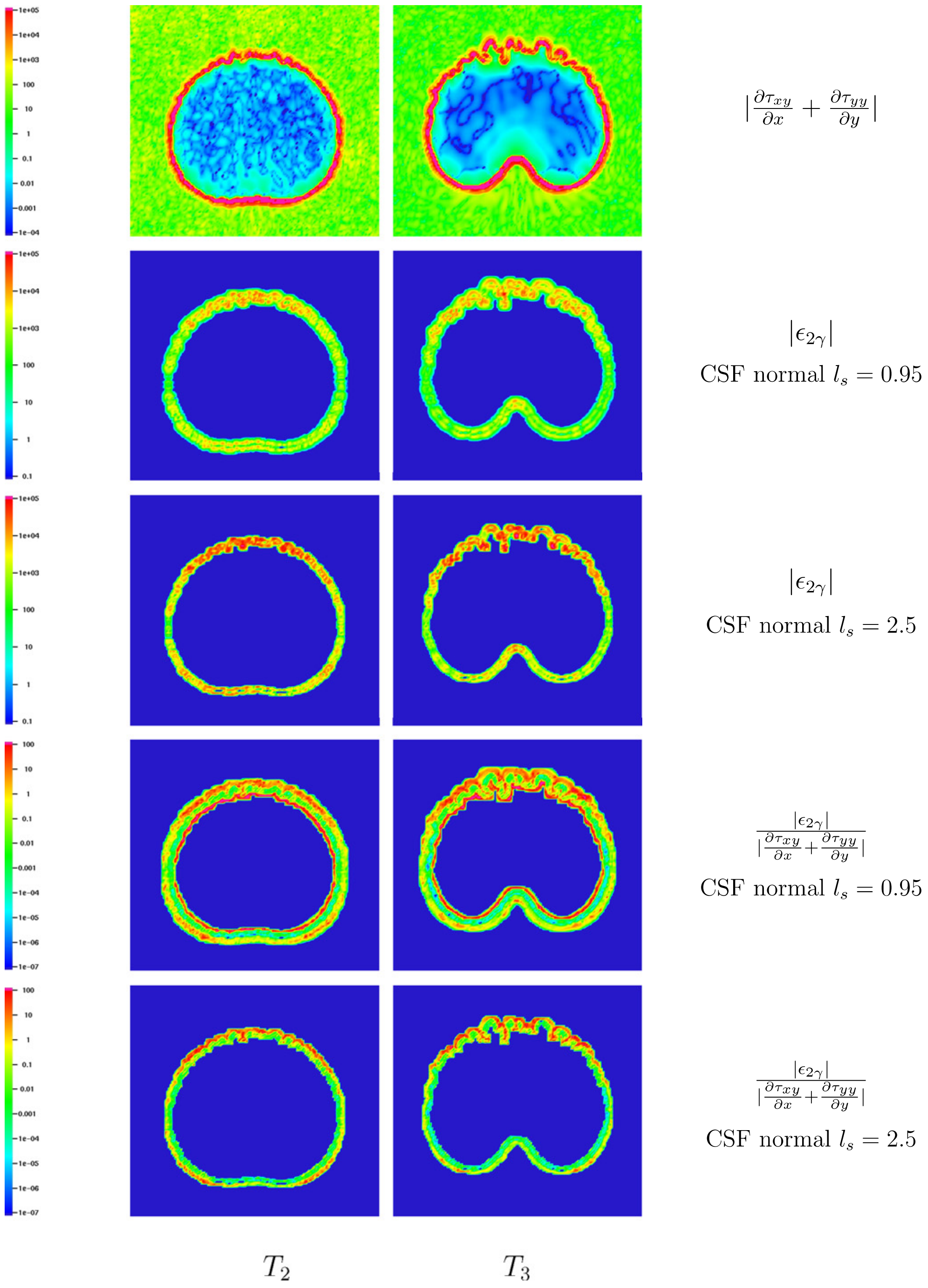

Fig. 1. Distributions resulting from *a priori* evaluation applied to DNS results of 2D bubble rise: row 1 quantifies the classical SGS stress term I, rows 2 and 3 show the unresolved surface tension term IV, and rows 4 and 5 show the ratio of the unresolved surface tension and SGS stress terms. Two sets of results are presented, based on different kernel smoothing lengths for our CSF-based interface normal computation.

unresolved surface tension in Fig. 1 suggests that it may become increasingly significant for flows featuring fluid scales tending towards the subgrid-scale. The explicit subgrid-scale modelling of the unresolved surface tension term is currently being pursued, but for the time being remains elusive. Even modern surface tension discretization schemes (such as the ghost fluid-based sharp surface force (SSF) method of Francois et al. [24]) tend to cause parasitic currents that do not disappear with mesh refinement. In modelling of turbulence SGS stresses, we seek to mimic the unresolved part of the energy cascade down to the Kolmogorov length scale. For the unresolved surface tension part, SGS modelling firstly requires the minimum length scale of interface deformations be quantified, and whether this really has an impact on the energy spectra of the resolved field ascertained. Even if underresolved interfacial scales indeed have no effect on turbulence, they nonetheless constitute a contribution to interfacial surface area that needs to be addressed. As such, it is clear that all relevant interaction mechanisms involving non-resolved interface and turbulence scales need to be clarified, before versatile models can realistically be formulated. On a final note, the origin of parasitic currents in VOF-based balanced-force solution algorithms (of the type introduced by Francois et al. [24]) is asserted to solely be error in curvature estimation. As such, filtering generating subgrid-scale terms including unresolved curvature, and adequate closures for these terms, may contribute to the elimination of parasitic currents generated by surface tension models.

4.2. Modelling of the SGS stress term

The effect of turbulence small scales on the supergrid scale flow solution appears through the phase-specific SGS tensor, defined in Eq. (16), which should be modelled. If the non-resolved velocity $u'_i = u_i - \overline{u_i}$ is defined, the SGS stress can be decomposed into three parts: $\tau_{ij} = \bar{\rho}(L_{ij} + C_{ij} + R_{ij})$, where L_{ij} is the Leonard term, C_{ij} is the cross-scale term, and $R_{ij} = \overline{u'_i u'_j}$ is the true SGS Reynolds stress. The deviatoric part of R_{ij} is the only quantity that needs to be modelled, using for an example an eddy viscosity model.

The LES approach employed in the solution algorithm is based on explicit SGS modelling within the eddy-viscosity framework, where R_{ij} is made proportional to the resolved strain rate $\overline{S}_{ij}$ via the eddy viscosity ν_t, i.e.

$$\tau_{ij} = -2\nu_t \widetilde{S}_{ij} + \delta_{ij}\tau_{kk}/3. \tag{18}$$

In the presence of shear, be it near the wall or in the vicinity of deformable surfaces where the viscous sublayer is well resolved, eddy viscosity models generally need to incorporate a damping function in order to accommodate the near-wall/interface limiting behaviour under low-*Re* number flow conditions. This is usually achieved by the incorporation of the Van Driest damping function in front of the length scale. Similar 'corrections' obviously need to be introduced in the case of the model being employed for interfacial two-phase flows, where the lighter phase perceives the surface like a rigid wall. The extensive DNS of counter-current two-phase flow studies of Fulgosi et al. [6] have indeed revealed the need for turbulence damping approaching deformable interfaces in the under-resolved simulation of such flows, very much in the same way as for wall flows. A systematic LES study of Fulgosi's [6] flow performed in [5] has shown that without that modification, the Smagorinsky model alone becomes excessively dissipative – also very much in the same manner as in wall-bounded flows.

In the present, we have used the definition below for the eddy viscosity

$$\nu_t \equiv \ell^2|\overline{S}| = f_{\mu\mathrm{Int}}(C_s\overline{\Delta})^2(2\tilde{S}_{ij}\tilde{S}_{ij})^{1/2}, \tag{19}$$

where length scale $\ell = \sqrt{f_{\mu\mathrm{Int}}}(C_s\overline{\Delta})$ is based on the cell size $\overline{\Delta}$, and with the value of the model coefficient set to $C_s = 0.1$ in the core flow. This value is somewhat smaller than the conventional value determined from isotropic decay of turbulence, i.e. $0.15 < C_s < 0.22$. In this new multi-fluid flow context, it is understandable that the model coefficient value could be inferred only by reference to wall flows, or, in a certain measure, from known DNS or LES multiphase flow data. Earlier LES of bubbly flow studies of Milelli et al. [20] using the dynamic SGS approach of [4] have indeed shown the C_s value to converge towards 0.1, with relatively small scatter; a value which has since then been used in our model. The damping model function $f_{\mu\mathrm{Int}}$ has been inferred from the DNS database of Fulgosi et al. [6]. For low to moderate interface deformations, the DNS data provide an exponential dependence of $f_{\mu\mathrm{Int}}$ on the normalized distance to the interface y^+_{Int} from the gas side:

$$f_{\mu\mathrm{Int}} = 1 - \exp(-0.00013(y^+_{\mathrm{Int}}) - 0.00036(y^+_{\mathrm{Int}})^2 - 1.08E^{-05}(y^+_{\mathrm{Int}})^3). \tag{20}$$

Analogous to the concept of a "wall units" length scale used in near-wall turbulence SGS and RANS modelling, the damping of eddy viscosity in SGS models close to deformable interfaces uses its own "interface turbulence units" length scale, denoted here by y^+_{Int}. We will next show how to extract the ingredients from the flow necessary to estimate this length scale – namely the interfacial shear velocity U_τ, and the distance to the interface ϕ. On a final note, the DNS of Fulgosi et al. [6] captured shear-induced interface deformation as well the physically correct near-interface turbulence behaviour.

5. Multi-physics modelling at deformable interfaces

5.1. Reconstructed distance function (RDF)

The distance function, the usual initialized quantity for the level set method [7] and particularly useful for flow physics modelling featuring proximity dependence, is not a natural output of VOF schemes. A new numerical scheme has been developed in this work for generating a reconstructed distance function (RDF) from VOF data, without having to advect the distance function using a hyperbolic level set equation. This scheme ensures that the distance function is consistent with the VOF representation of the interface, and that the advection of the distance function benefits from the conservation and robustness properties of volume tracking. Finally, it represents an easy way to implement interface proximity-dependent physics in established VOF-based codes, without the implementation and testing cost associated with removing the existing VOF infrastructure of an existing code and replace it with modern versions of level set-based interface tracking.

5.1.1. Base algorithm

The first scheme for RDF generation, developed by Cummins et al. [16], was documented as a 2D scheme for applications such as dendritic solidification and surface tension modelling. For these applications, the RDF needs to be computed on a compact support about the interface – two to three cells thick either side. For the purpose of near-interface multi-physics modelling, the distance function must resolve the full range of any local treatment. RDF generation for the current work therefore faces unique challenges:

(1) In resolving a near-interface region of a constant thickness, the mesh-cell thickness of the support scales with $1/\delta x$, and the number of mesh cells for which the RDF must be computed scales with $1/\delta x^3$. For other applications that use a constant mesh-cell support thickness, the number of cells for which the RDF must be computed scales with $1/\delta x^2$.
(2) The thickness of the near-interface region is dependent on the shear velocity, which varies across the interface with local flow conditions at any point in time.
(3) In the case of wide supports and convex surfaces, sweeping through the interface cells as the outer-loop sweep, and then growing the interface outwards, is not ideal.
(4) Interface/turbulence interactions leading to surface wrinkling and micro-breaking as well as interphase scalar transfer require reliable RDF computations for high-curvature sections of interfaces.

In the piecewise planar interface reconstruction step of 3D VOF schemes, coordinate data are generated in 3D space for each intercept of the interface reconstruction with the edges of its mesh cell; the centroid of the interface plane is then easily extracted from the intercept data. Fig. 2a shows sample interface reconstructions in two adjacent cells generates 12 points in space (10 intercepts and 2 centroids). This represents an abundance of interface coordinate data from which to create the RDF, and is stored in a list of interface markers. Fig. 2a shows all the lines of shortest distance between each interface point, and the mesh cell center on the flow solver mesh for which the reconstructed distance function value $\phi^{\mathrm{RDF}}_{i,j,k}$ is being generated.

Intercepts represent valid points for use in distance function reconstruction, and indeed are necessary for computing the centroid point of any VOF interface plane. However, the use of intercepts represents an increase in computation of twofold or more. Intercepts of a PLIC-VOF interface reconstruction may often be closer to cell center location (i,j,k) than the centroid from the same plane, but the locations of intercepts are also sensitive to plane orientation. In contrast, the VOF plane centroid is far less sensitive to changes from

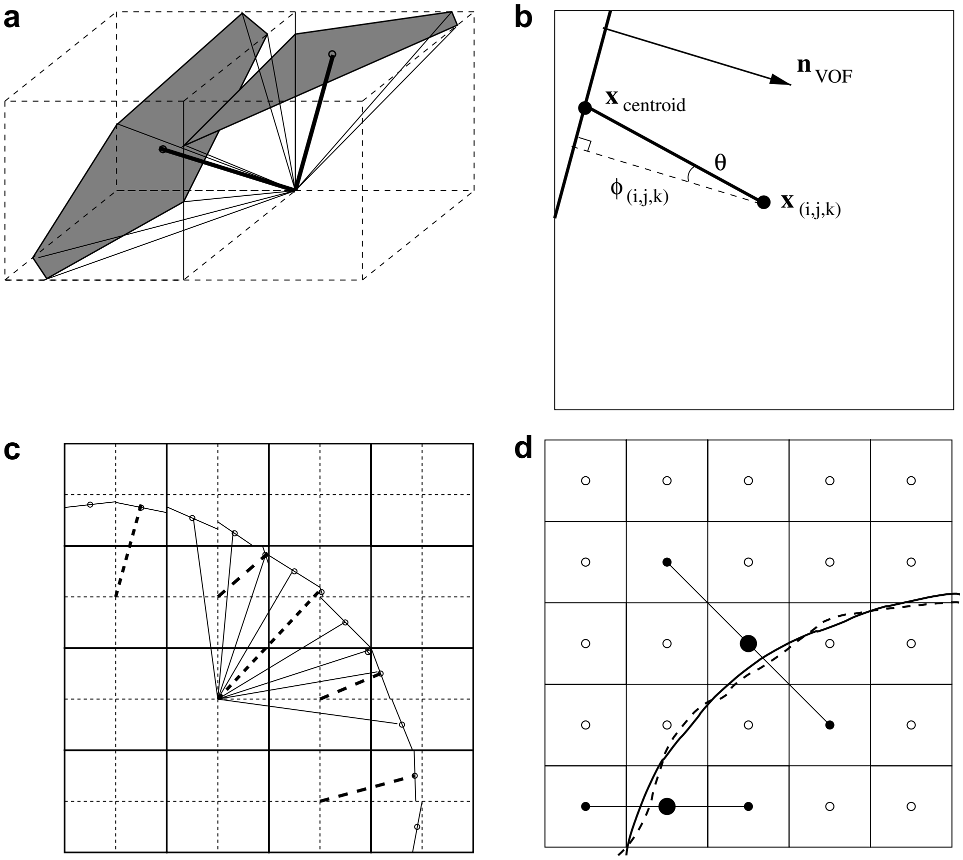

Fig. 2. The generation of the reconstructed distance function (RDF) data about 3D interfaces: (a) centroid and intercept data available as a by-product of the CVTNA interface reconstruction scheme; (b) moderation of the distance between a CVTNA data point and the mesh point using a cosine term prescribed by the VOF interface normal; (c) search for the CVTNA data point nearest to the mesh point (i,j,k), and enhanced accuracy using mesh refinement in VOF; (d) arithmetic averaging for RDF tautening in the immediate vicinity of the interface.

first-order to second-order interface reconstruction, with the point essentially acting as a pivot as $C_{i,j,k} \rightarrow 0.5$. For these reasons, our approach to RDF generation focuses on centroid data, and ignores intercept data.

To compute ϕ_{RDF} using a single interface marker approach to RDF generation, a sweep of a list of VOF interface coordinate data is performed, and the point resulting in the shortest distance to point (i,j,k) is identified. The list of VOF coordinate data is truncated to a small subset of the total population of data points to promote efficiency. Fig. 2b shows the line between the nearest interface point and point (i,j,k) to not be parallel to the VOF interface normal. We compute the angle between the two lines to be θ, and propose the following form for the θ-dependence of ϕ^{RDF}:

$$\phi^{\mathrm{RDF}}_{i,j,k} \approx |(\mathbf{x}_I - \mathbf{x}_{i,j,k})\cos\theta|, \tag{21}$$

where $\mathbf{x}_I$ is the interface marker. The interface marker is the intercept or centroid closest to point (i,j,k); in the example of Fig. 2b, the use of a centroid point is illustrated.

While Fig. 2b presents a persuasive geometric motivation for incorporating θ-dependence into ϕ^{RDF} estimates extracted from shortest distances between mesh points and VOF interface plane nodes, Eq. (21) only represents a model for this dependence. In the 2D approach proposed by Cummins et al. [16], upon the explicit extraction of the point on the PLIC-VOF interface computation closest to mesh point (i,j,k), stencil-based near-vicinity averaging (using a $|\cos\theta|^a$ dependence, $20 < a < 30$) and subsequent kernel smoothing over a 3δ support is used to reduce high-frequency errors and bound the errors on $\nabla\phi$. As well as promoting efficiency by avoiding the explicit computation of the shortest distance between (i,j,k) and the VOF interface plane through the use of by-products such as the interface centroid, the current scheme avoids the expense of the stencil-based averaging and kernel smoothing operations used in [16] in the following manner.

5.1.1.1. VOF mesh refinement. The use of VOF on the twice-as-fine mesh in the flow solver is used to improve RDF accuracy, beyond that achievable when the VOF mesh is resolved on the underlying flow solver mesh. As shown in Fig. 2c, refinement in the VOF mesh substantially reduces the size of discontinuities between planes in adjacent interface cells, and allows for a rudimentary capturing of interface SGS curvature. The capturing of SGS curvature is particularly desirable for high-curvature interface regions in turbulent flow.

5.1.1.2. Tautening about the zero level of the RDF. Most of the errors in ϕ and $\nabla\phi$ occur in the immediate vicinity of the interface – noise on otherwise smooth zero ϕ-levels. These errors in both ϕ and $\nabla\phi$ drop rapidly moving away from the interface, and as $\theta \to 0$ in Eq. (21). We are able to use these better ϕ estimates one to two cells away from the interface to tauten the RDF about the zero level, by approximating orthogonal trajectories across the 3D zero level surface with single lines between mesh points. In this tautening procedure, the normal of an interface cell (i,j,k) is used to identify a line between mesh points on opposite sides of point (i,j,k) within a 27-cell stencil, that best approximates the trajectory prescribed by the interface normal. Arithmetic averaging between the points either side of (i,j,k) is then used to generate an alternative estimate ϕ'^{RDF} at this point. For smooth distance functions with normals coinciding with these crude orthogonal trajectory reconstructions, this alternative estimate would match the original ϕ^{RDF} estimate generated using Eq. (21). For normals deviating from $n\pi/2$ trajectories through the xy, xz or yz planes, smooth distance functions would only result in small discrepancies between the original estimate and ϕ'^{RDF}; we use this property to detect excessive error in the single-marker estimate generated using Eq. (21). In the immediate vicinity of the interface, the RDF is modified to the alternative estimate ϕ'^{RDF} if the discrepancy between the original and alternative is large, which we define to be a fraction of a mesh cell breadth (e.g. 0.1Δ, where $\Delta = \sqrt{\delta x \delta y}$ is used in the case of tautening between $(i-1,\ j-1,\ k)$ and $(i+1,\ j+1,\ k)$). Fig. 2d illustrates noise in the original RDF construct of the zero level, and the manner in which arithmetic averaging between mesh points can reduce this noise. The tautening procedure does a better job in localizing ϕ modification to the interface than kernel smoothing, and is much more efficient and ensures RDF generation is possible over less-than-compact interface supports.

5.1.2. RDF tests

To test our RDF scheme, we use the problem of reconstructing the distance function on both sides of a spherical shell interface. The sphere is of radius 0.25 and is centered at (0.5, 0.5, 0.5). The RDF is computed for all cells within a distance of 0.1 of the interface. Table 1 lists the combinations of options used in the numerical experiments. Five variants are used to assess the respective merits of using the twice-as-fine VOF mesh, of neglecting the use of interface reconstruction intercept data, and of tautening in the immediate vicinity of the zero level. For that purpose, two error norms are introduced for ϕ^{RDF} and $|\nabla\phi^{\mathrm{RDF}}|$, defined as:

$$L_2(\phi) = \sqrt{\frac{1}{V}\int_V (\phi^{\mathrm{RDF}}_{i,j,k} - \phi^{\mathrm{exact}}_{i,j,k})^2\,\mathrm{d}V} \approx \sqrt{\frac{\sum_{l=1}^{N}(\phi^{\mathrm{RDF}}_l - \phi^{\mathrm{exact}}_l)^2}{N}}, \tag{22}$$

Table 1
Schemes, meshes and data used to generate reconstructed distance function ϕ^{RDF}

	VOF interface reconstruction	Plane points	VOF mesh	Interface tautening
Variant 1	CVTNA	Centroid	Normal	No
Variant 2	CVTNA	Centroid	Normal	Yes
Variant 3	CVTNA	Intercepts + centroid	Normal	Yes
Variant 4	CVTNA	Intercepts + centroid	Twice-as-fine	Yes
Variant 5	Youngs gradient	Centroid	Twice-as-fine	Yes

$$L_\infty(\phi) = \max_{(i,j,k)\in V}(\phi^{\mathrm{RDF}}_{i,j,k} - \phi^{\mathrm{exact}}_{i,j,k}) \approx \max_{l\in N}(\phi^{\mathrm{RDF}}_{l} - \phi^{\mathrm{exact}}_{l}), \tag{23}$$

where V is the near-interface region of thickness 0.1 either side of the interface, and l is a cell of this region. Similar formulae are used for computing $L_2(|\nabla\phi|)$ and $L_\infty(|\nabla\phi|)$ as well, with standard centered differences on a 7-cell stencil used to estimate $\nabla\phi$. The error norms are written in this way assuming a constant width of the near-interface region.

Fig. 3 shows the results obtained using each scheme variant for RDF generation. Second-order accuracy on ϕ is achieved on $L_2(\phi^{\mathrm{RDF}})$, whereas the accuracy with refinement on $L_\infty(\phi^{\mathrm{RDF}})$ is no better than first-order. The departure from second-order accuracy is a symptom of high-frequency errors as noted by Cummins et al. [16]; the magnification of these high frequency errors upon differencing is also seen in Fig. 3. In the results shown, the convergence of $L_2(|\nabla\phi^{\mathrm{RDF}}|)$ and the high-resolution deviation from convergence in $L_\infty(|\nabla\phi^{\mathrm{RDF}}|)$ suggest the high-frequency errors are concentrated locally near the zero level, rather than uniformly through the support. The general convergence shown demonstrates the ability of our approach to generate RDF distributions through less-than-compact interface supports that complement the VOF representation of the interface using simple, computationally inexpensive operations. The approach of Cummins et al. [16] can also be incorporated for RDF generation in the immediate vicinity of the interface; alternatively, multiple applications of the cheap tautening procedure may be able to achieve the same noise reductions in the vicinity of the zero level. In terms of absolute accuracy, the improvements attained using the twice-as-fine mesh, higher-order VOF interface reconstruction and tautening are evident, while ignoring intercept data is not detrimental at all.

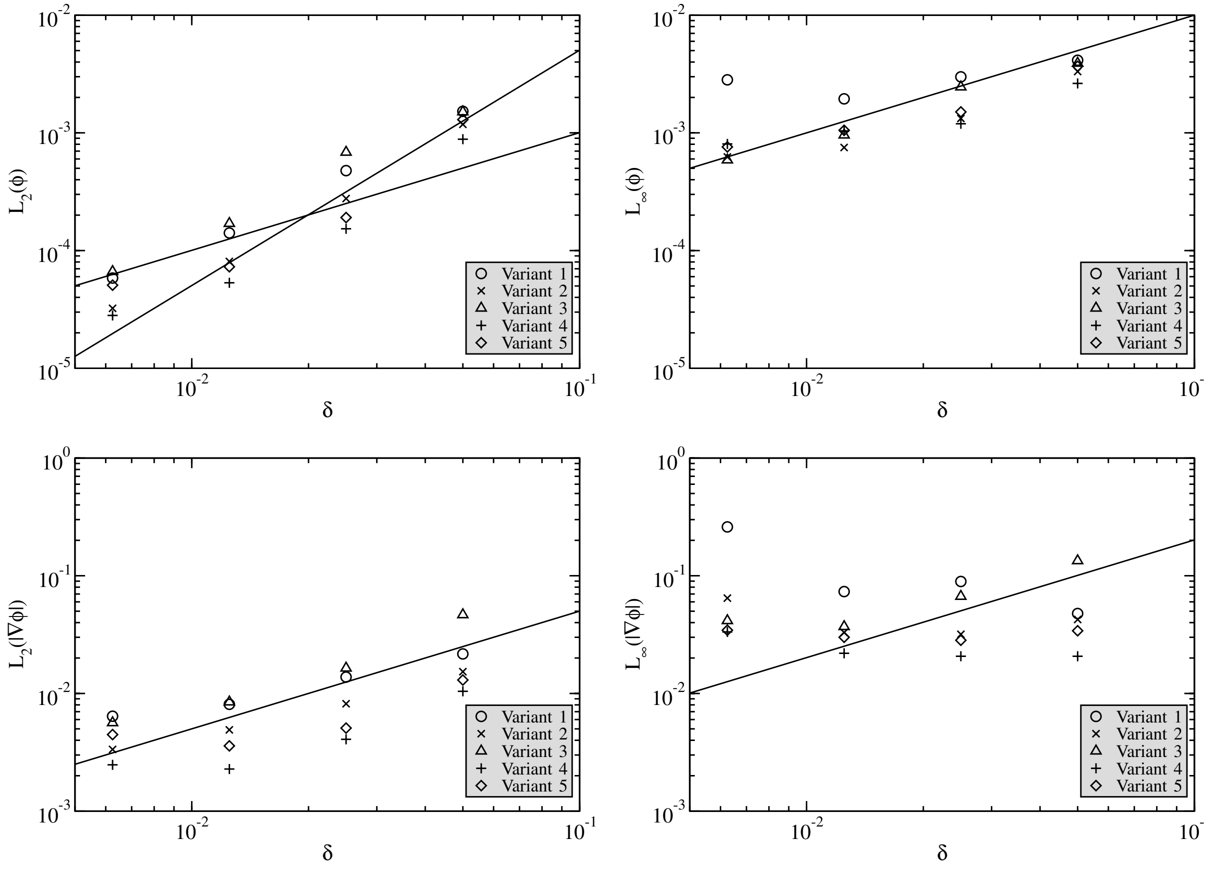

Fig. 3. Errors associated with the generation of the RDF throughout a support of thickness $\Delta = 0.1$, for a sphere of radius 0.25 and centered at (0.5, 0.5, 0.5) in a $1\times1\times1$ domain. Results are presented for the RDF-generation variants listed in Table 1.

5.1.3. RDF generation and existing level-set methodologies

Planar interfaces and $\phi = 0$ are noted here to be sharp representations of interfacial fronts in volume-of-fluid and level set methods, respectively. Additional commonality with level set methods is identified here in the core step of RDF generation – the computing of distances from mesh points to the planar VOF interface front. This is because a similar task is a feature of the original "direct" re-initialization procedure introduced to level-set methods by Chopp [25]. The level-set literature tends to consider the direct re-initialization procedure to be time-consuming, which motivated Sussman et al. [26] to develop an alternative, iterative approach to re-initialization. Computational savings in such an iterative approach over direct re-initialization depend on how accurate and smooth the initial ϕ estimate is set throughout the interface support. If our RDF generation scheme commences only with VOF interface reconstruction data and with no knowledge of interface proximity, then the initial estimate from Sussman et al.'s approach is necessarily poor and of little potential utility. During the course of a transient simulation, however, ϕ^{RDF} values taken from a previous timestep may constitute a relatively good initial guess. This potentially allows the iterative approach to contribute to more efficient RDF generation throughout larger interface supports. Other concepts for re-initialization may similarly be able to supplement RDF generation, such as those based on the fast-marching method outlined in [27].

The level-set methodologies described above are able to supplement RDF generation by refining ϕ estimates without explicit distance computations to the interface front. In maintaining the use of VOF interface tracking and in the absence of explicit level-set advection, the need for RDF generation remains. Re-initialization using Sussman et al.'s iterative approach starts at the interface and moves outwards, and has the property of not changing ϕ at the interface. As such, the exercise of updating ϕ in the vicinity of evolving interface fronts remains essential, and remains the domain of RDF generation schemes for consistent coupling between the distance function and the VOF interface advection. Similarly, fast-marching methods rely on the initialization of the zero level set, and again rely on RDF generation for the interface front in the absence of explicit advection using the level-set equation. RDF generation with tautening for improved smoothness of ϕ at the interface remains essential for the narrow band of up to two mesh cells from the interface. Beyond that band, we do not consider the use of RDF generation through the wider support compulsory, and its use in preference to non-direct re-initialization approaches from level-set methods to be a choice based on implementation effort and performance.

5.2. Reconstructed interfacial shear velocity (RISV)

5.2.1. Base algorithm

The initial step of the scheme consists in performing a mesh sweep confined to a narrow (one cell thick) interface support. In this sweep, a list of interface points is identified, and the shear at each of these points is recorded. Throughout the narrow support, cell-centered points P are identified to the gas side of $\phi^{\mathrm{RDF}} = 0$. At any point P, a normal estimate is generated based on a standard level-set estimate $\hat{\mathbf{n}}_P^{\mathrm{RDF}} = \nabla\phi_P^{\mathrm{RDF}}/|\nabla\phi_P^{\mathrm{RDF}}|$. Tracing back along $\hat{\mathbf{n}}_P^{\mathrm{RDF}}$ generates the interface marker I estimate (x_I, y_I, z_I), defined as

$$\mathbf{x}_I = \mathbf{x}_P - |\phi_{i,j,k}^{\mathrm{RDF}}|\hat{\mathbf{n}}_P^{\mathrm{RDF}}. \tag{24}$$

Note that the interface normal can, in principle, be imported from the piecewise planar interface reconstruction scheme in the VOF algorithm. The more accurate normal estimates from the VOF interface reconstruction could promote accuracy in interfacial shear computation, but has not been used here because: (i) the existing VOF data are generated on a twice-as-fine mesh, hence making it inconvenient to attempt to generate regular-mesh VOF normals, and (ii) the scheme presented here is intended for general applicability to non-VOF flow solvers, using either distance function data from level-set interface trackers, or RDF data generated from non-VOF interface tracking schemes.

To generate shear estimates over the entire interface, it is necessary to compute the velocities at interface markers I, and their corresponding gas-sided mesh points P (denoted hereafter as $\mathbf{U}_I$ and $\mathbf{U}_P$, respectively). Interface marker I will generally not align with the spatial locations of velocity information on meshes (as shown in Fig. 4a), thus making it impossible to linearly extrapolate mesh-based velocity information to an arbitrarily located interface marker. To overcome this difficulty associated with arbitrarily and massively deformable interfaces, we introduce an approach to estimating $\mathbf{U}_I$ that involves extrapolating along logically-connected lines of adjacent mesh points to a number of nearby points surrounding point I, then interpolating from these surrounding points to I. Given the location of point I and the component (u_I, v_I, w_I) of the velocity vector that needs to be computed, separate sets of lines enclosing interface marker I are identified. Figs. 4a and b show a set of two lines is required to enclose an interface marker in 2D space, while Fig. 4c shows a set of four lines is required to enclose a marker in 3D space. Figs. 4a and b show the staggered-mesh scenario, in which a different set of lines needs to be defined for computing each component of $\mathbf{U}_I$. Our approach of extrapolating along lines to the interface then interpolating to markers is even easier for collocated orthogonal meshes.

To identify the appropriate set of lines for enclosing point I, we firstly identify the dominant component of the interface normal that has been computed for the accompanying point P; $\max(\hat{n}^x_P, \hat{n}^y_P, \hat{n}^z_P)$ is used to identify the direction in which the lines extend. This choice for setting the direction is dictated by our desire for logical

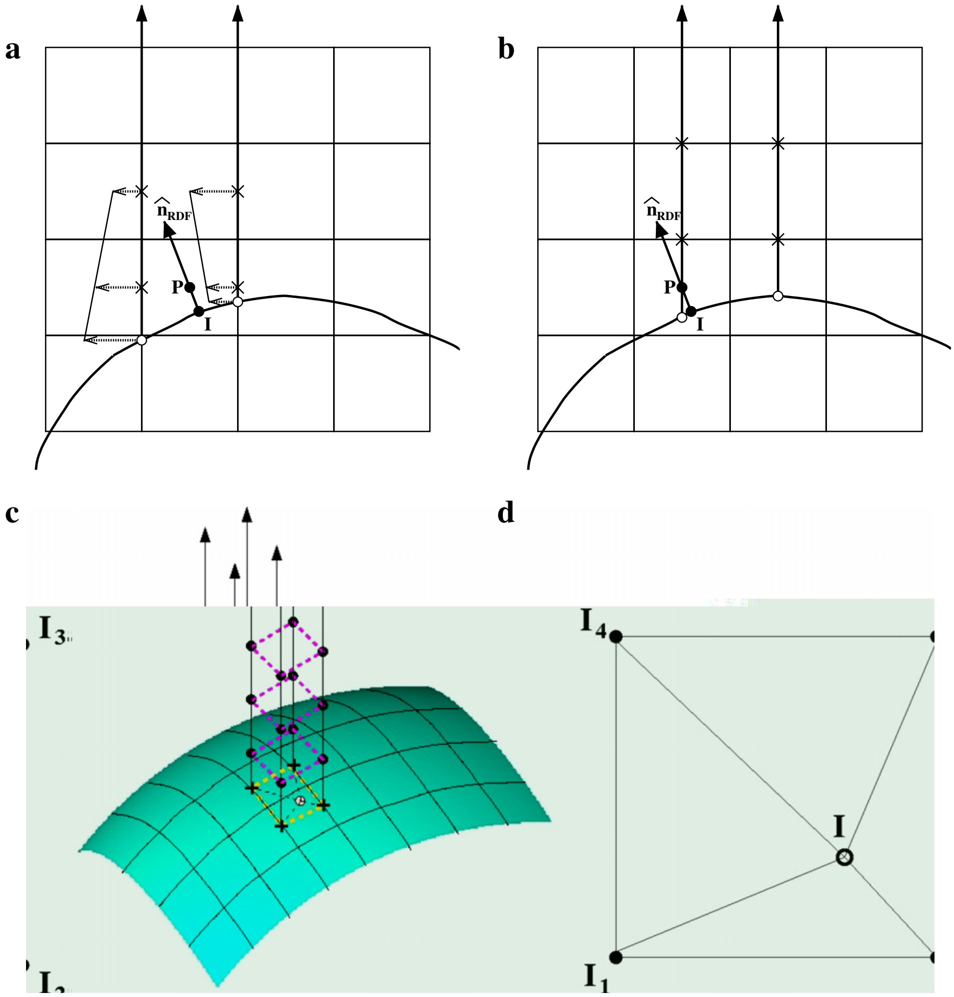

Fig. 4. Layout of staggered-mesh velocity data for the extrapolation of gas-sided velocities to the interface. Given the interface marker I and knowing the dominant component of the interface normal, the lines of adjacent cell-face points that surround point I are identified and projected into the gas phase. (Panels (a) and (b) show different points are used for generating estimates to different velocity components on staggered meshes.) The gas-sided extrapolation takes places along these rods to the interface. The rod-interface intercepts enclose curves (in 2D) or ruled surfaces (in 3D); the velocities at these vertices are then used to estimate interface marker velocity $\mathbf{U}_I$.

robustness. For linear extrapolation, the nearest two mesh points along the line extended back from the interface must reside in the gas phase. If the surface is concave, extending lines in the dominant direction ensures enough gas-sided mesh points, by reducing the chances of the interface folding back to intersect between the first and second points back from the interface along the rod. Fig. 4a shows an example of line generation for estimating u_I, with $+\hat{n}^y$ being dominant, and lines of $(i+1/2,j)$ data points extending in the direction of increasing j, while estimating v_I uses lines of $(i,j+1/2)$ data points extending in the direction of increasing $j+1/2$.

Fig. 4c shows the intersections between the lines and the interface to be the vertices of a ruled surface, which represents the small segment of the entire surface area upon which interface marker I is located. Fig. 4d shows a logical rectangular representation of the ruled surface, with vertices I_1 to I_4, and the interface marker I located in the same relative location as in Fig. 4c. The interface velocity estimates at I_1 to I_4 are subsequently interpolated to I using an inverse distance-based interpolation

$$\mathbf{U}_I = \frac{\frac{1}{d_{I1}^p}\mathbf{U}_{I1} + \frac{1}{d_{I2}^p}\mathbf{U}_{I2} + \frac{1}{d_{I3}^p}\mathbf{U}_{I3} + \frac{1}{d_{I4}^p}\mathbf{U}_{I4}}{\frac{1}{d_{I1}^p} + \frac{1}{d_{I2}^p} + \frac{1}{d_{I3}^p} + \frac{1}{d_{I4}^p}}, \tag{25}$$

where distances between line-interface intercepts I_a and interface marker I, $d_{Ia} = |\mathbf{x}_{Ia} - \mathbf{x}_I|$, are raised by default to the power $p = 1$. (Bilinear or an alternative interpolation may be another possibility here, but is not used in the current work.)

The procedure described for computing $\mathbf{U}_I$ is also used to generate a velocity estimate at point P, to avoid contamination of the velocity estimate by liquid-side gradients. Vector resolution is used to extract the components of $\mathbf{U}_P$ and $\mathbf{U}_I$ that are parallel and perpendicular to the interface normal:

$$\mathbf{U}^{\text{shear}} = \mathbf{U} - (\mathbf{U}\cdot\hat{\mathbf{n}})\hat{\mathbf{n}}. \tag{26}$$

The present model for estimating the shear stress at the arbitrarily located and oriented interface presumes mesh cell point P is close to the interface marker I – equivalent to resolving the viscous sublayer near rigid walls. When the near-interface regions are well resolved, the shear velocity gradient is estimated using the one-sided finite difference

$$\frac{\mathrm{d}\mathbf{U}_P}{\mathrm{d}n} = -\frac{\mathbf{U}_P^{\text{shear}} - \mathbf{U}_I^{\text{shear}}}{\mathbf{x}_P - \mathbf{x}_I}, \tag{27}$$

and the shear stress at interface marker I is computed as

$$\tau_I = -\mu\frac{\mathrm{d}\mathbf{U}_P}{\mathrm{d}n}. \tag{28}$$

The list of $(\mathbf{x}_I, \tau_I)$ entries from the first, narrow-support sweep through the mesh is kept to complete the computing of the near-interface turbulence damping.

5.2.2. The interfacial sublayer: "interface wall unit"

The thickness of the near-interface support is dependent on local flow conditions in the vicinity of the surface, and will vary in space and time across all interfaces evolving in the flow. In the second part of the scheme, a wider support is flagged on the gas-side of the flow, and the flow/turbulence properties relevant to the physics in question (turbulence damping in the current case) are computed at all cell-center points P located in the support.

Tracing back from point P distance ϕ^{RDF} along the trajectory prescribed by the level-set normal $\hat{\mathbf{n}}_P^{\text{RDF}}$ ends at a point in space $\mathbf{x}_{I'}$. Given knowledge of smooth and accurate level sets based on ϕ, point I' is located on an interface, but will not exactly coincide with the location of any interface marker I stored in the list from the first mesh sweep. The interfacial shear stress at point I' is interpolated from the list of $(\mathbf{x}_I, \tau_I)$ entries; inverse-distance weighting is used here again:

$$\tau_{I'} = \sum_a \frac{1}{d_a^p}\tau_{Ia} \Big/ \sum_a \frac{1}{d_a^p}, \tag{29}$$

where $d_a = |\mathbf{x}_{Ia} - \mathbf{x}_I|$ and I_a represents an interface marker in the list, and $p = 1$. Eq. (29) is a simple interpolation of the τ_I list entries to point I', that is most valid over a relatively small surface area about that point.

Using the shear velocity $U_\tau = \sqrt{\tau_{I'}/\rho_G}$, the non-dimensional distance of point P from the interface is computed as

$$y_P^+ = y_{\text{Int}}^+ = \rho_G U_\tau |\phi_P^{\text{RDF}}|/\mu_G. \tag{30}$$

While it is preferable the support about I' for Eq. (29) be small, a very small support about I' has been found to introduce unrealistic roughness in contours of the near-interface turbulence length scale. The problem application is a factor that influences the maximum feasible size of the support about I'. As an example, for many free surface flows, the interface normal generally points upwards, and cases of including interface markers that result in large arc lengths between I' and I_a despite small separations in 3D space are not important.

Fig. 5 shows that Eq. (20) prescribes damping up to $y_{\text{Int}}^+ \approx 70$. Using this cutoff on y_{Int}^+ provides an indication of the width of the interface support that must be accommodated in the second sweep. Storing $U_\tau^{\min}$ from the previous time step, the estimate on $\phi_{\max}$ that must be included in the interface support can be estimated as

$$\phi_{\max} < c\frac{\nu y_{\text{Int}}^+}{U_\tau^{\min}}, \tag{31}$$

where factor c accounts for changes in the flow from one time step to the next (say $c \approx 1.5$). Given the dependence of y_{Int}^+ on local flow conditions, the necessary width of interface support for defining the RDF may fluctuate significantly during the simulation.

In principle, near-interface regions from two opposite interfaces, based on different shear velocity estimates, can be visualized to overlap. In the current implementation, the interface normal is the primary driver for identifying the segment of interface a certain mesh point “belongs to”. After the main y_{Int}^+ computation, abrupt changes in the y_{Int}^+ scale and unphysical values are detected, and are taken to be locations of overlapping interface regions in proximity to multiple proximate faces from separate closed bodies. In the vicinities of such locations, multiple y^+ candidates based on tracing to the different interfaces are generated, and the minimum of all candidate values is used to ensure damping:

$$y_{\text{Int}}^+ = \min\left(y_1^+, y_2^+, \ldots, y_n^+\right), \tag{32}$$

where n is the number of potential values based on RISV extrapolation from different interfaces. In reality, the multiple interfaces in the vicinity of the same point share the same flow field, which suggests the spread of candidate values for y_{Int}^+ will not be large: the surface smoothing of τ_I and the weighting of Eq. (29) contribute to the small spread of the candidate y_{Int}^+ values.

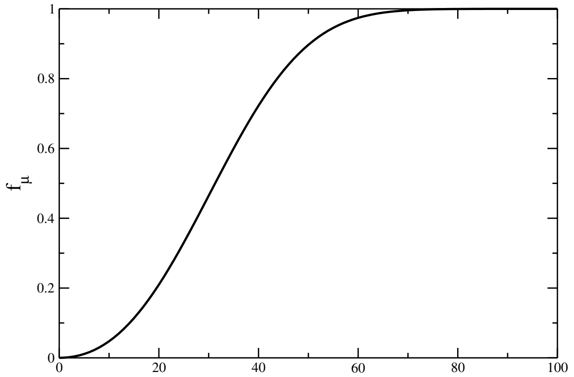

Fig. 5. Turbulence damping approach a deformable interface from the gas side, as prescribed by empirical correlation generated from the DNS database of Fulgosi et al. [6] for low wave deformation (Eq. (20)).

5.2.3. Tangential annular Newtonian fluid flow

As a test to verify and validate the interfacial shear determination scheme presented above, we use the tangential annular flow of a Newtonian fluid of presented by Bird et al. [28]. The solution to the velocity field in cylindrical coordinates, $\mathbf{u} = (v_r, v_\theta, v_z)$, is

$$v_\theta = \Omega_0 R \frac{\left(\frac{\kappa R}{r} - \frac{r}{\kappa R}\right)}{\left(\kappa - \frac{1}{\kappa}\right)}, \tag{33}$$

where Ω_0 is the circumferential velocity, κ is the ratio of the inner to outer radius, R is the outer radius, and r is the radial coordinate. For anti-clockwise flow, the velocity field in Cartesian coordinates $\mathbf{u} = (u, v, w)$ is

$$u = -v_\theta \sin\theta \quad \text{and} \quad v = v_\theta \cos\theta. \tag{34}$$

Fig. 6 shows the substantial shear in the velocity field for increasing distance from the axis of symmetry. Here we set $\Omega_0 = 1$, $R = 0.25$ and $\kappa R = 0.05$. Using the analytical velocity field solution, we converge the shear stress solution at the $R = 0.25$ isosurface (which we adopt as the gas/liquid interface in the current test problem) to $\tau_I = 1.9608333 \times 10^{-5}$. In this test, we refer to the interface being concave when the gas phase occupies $r < R$ and the liquid phase occupies $r > R$, such that the prescribed turbulence modification is done inside the circular interfacial cross-section. When the interface is convex, turbulence modification is prescribed to surround a closed liquid body.

The tangential annular flow problem requires gas-sided extrapolation of velocities to the interface through the entire range of 2D interface orientations, making it a challenging test for any scheme that depends on interface orientation; the result for comparison here is τ_I. The first test performed involves imposing the analytical solution to ϕ, at both mesh cell-center (i,j,k) and cell-face $[(i+1/2, j, k); (i, j+1/2, k); (i, j, k+1/2)]$ locations, thereby removing the inaccuracies introduced by distance function reconstruction (for VOF-based solution algorithms in which the RDF is generated) or advection (for level set-based solution algorithms).

The left side of Figs. 7 and 8 shows τ_I results for the concave and concave interface cases, respectively, for the case of the exact distance function being imposed. The results are shown as a function of the azimuthal location of interface marker I relative to the problem initialization axis centered at (0.5, 0.5); given the problem initialization, the expected eight-fold symmetry was obtained through the whole 2π about the axis of rotation. When the exact distance function is imposed, the vast majority of unsmoothed results faithfully reproduce τ_I^{exact}. The deviations from τ_I^{exact} obtained at low resolutions are a result of inaccuracies introduced by the inverse distance-based interpolation between line estimates used in Eq. (25) for points I that are relatively close to one vertex or edge of the ruled surface shown in Fig. 4c–d. An alternative interpolation, or a well-investigated calibration of power p in Eq. (25) away from unity, may remove such visible deviations in the low-resolution results. The localized surface smoothing is effective in reducing these deviations in any case. Table 2 shows strong convergence if the distance function solution is exact, with averaged results seen to converge with second-order accuracy to within a fraction of a percent of the exact answer.

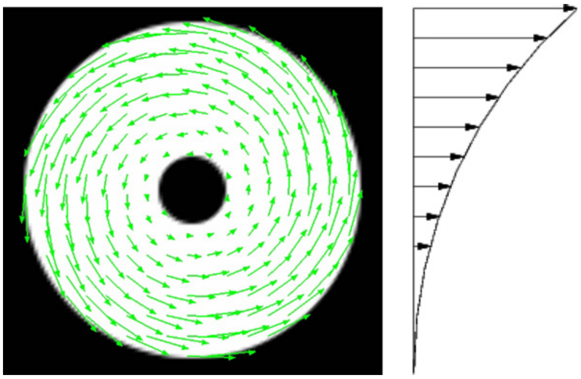

Fig. 6. Tangential annular flow test problem.

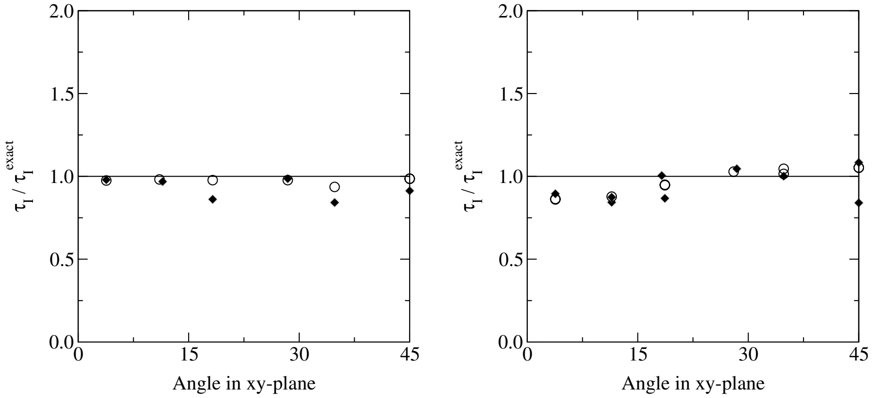

32× 32× 4

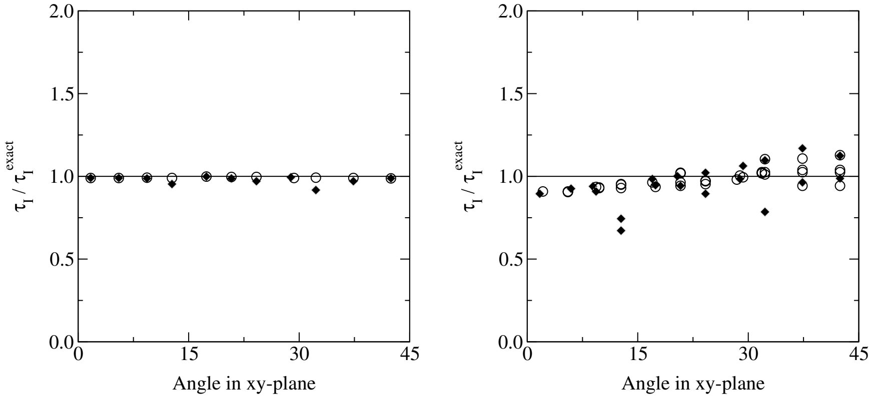

64× 64× 8

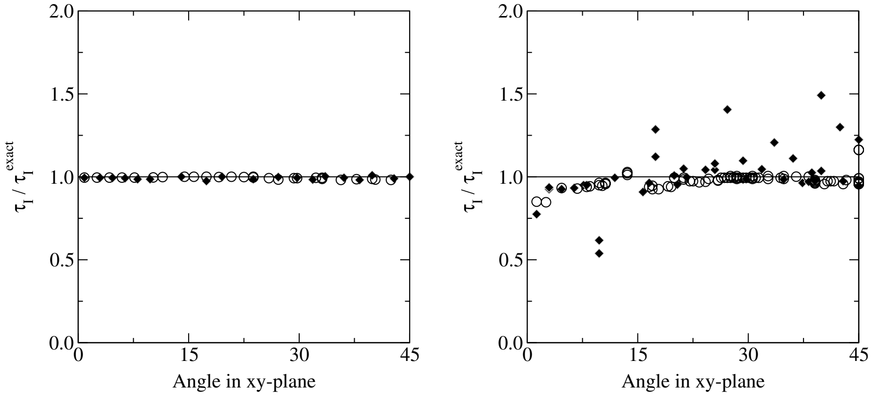

128× 128× 16

Fig. 7. Computed shear stresses (τ_I) to the concave (inner) side of the gas–liquid interface, for the problem of tangential annular flow. The results on the left are for the case of the analytical solution for the distance function being imposed, while the results on the right are for the case of the RDF generated from VOF data on a twice-as-fine mesh. The values denoted by ◆ represent τ_I generated prior to a localized surface smoothing operation, while the values denoted by ○ represent τ_I after the surface smoothing.

The right side of Figs. 7 and 8 shows the τ_I results for the case of the tautened RDF generated from CVTNA interface reconstruction data off a twice-as-fine VOF mesh. The comparison between the panels in the left and right columns shows the estimation of τ_I to be sensitive to errors in the distance function, and

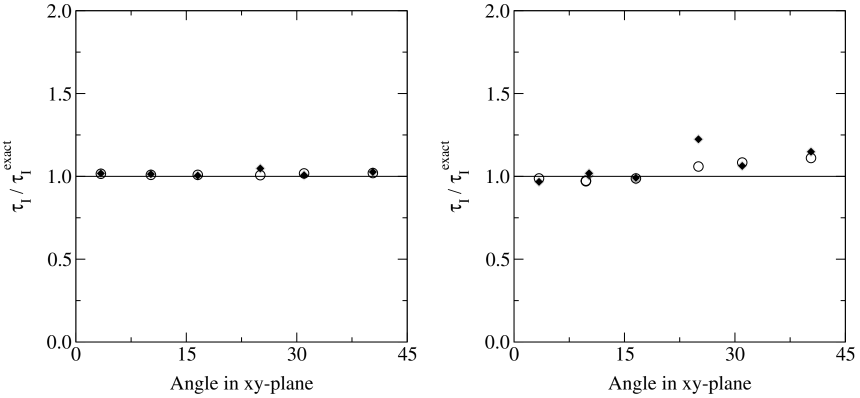

32× 32× 4

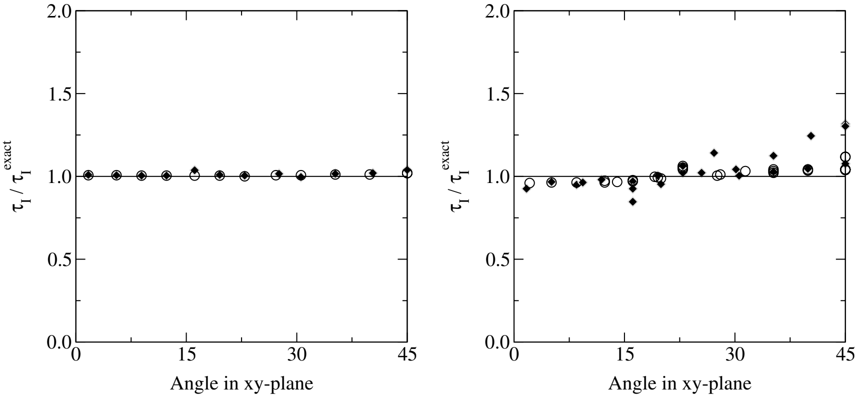

64× 64× 8

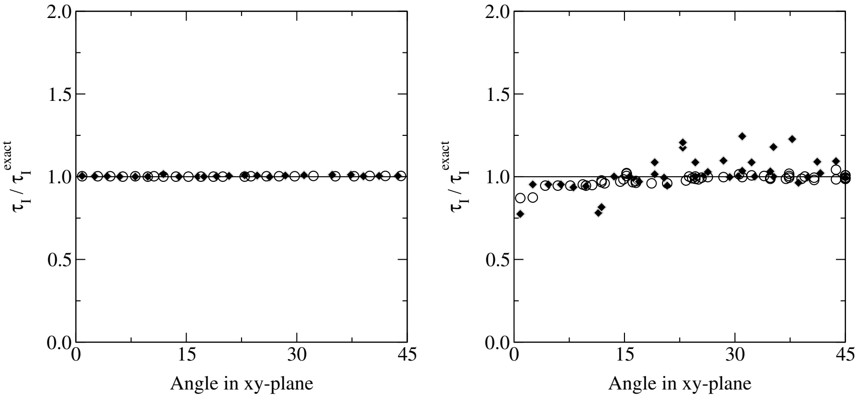

128× 128× 16

Fig. 8. Computed shear stresses (τ_I) to the convex (outer) side of the gas–liquid interface, for the problem of tangential annular flow. The results on the left are for the case of the analytical solution for the distance function being imposed, while the results on the right are for the case of the RDF generated from VOF data on a twice-as-fine mesh. The values denoted by ♦ represent τ_I generated prior to a localized surface smoothing operation, while the values denoted by ○ represent τ_I after the surface smoothing.

specifically to the high-frequency error in the immediate vicinity of the interface. Sensitivity to this high-frequency error is not necessarily surprising, given the use of the level-set normal in the RISV scheme and the observed lack of convergence in $L_\infty|\nabla\phi|$ in the RDF tests. Introducing the error measures on τ_I

$$L_2(\tau_I) = \frac{1}{\tau_I^{\text{exact}}} \sqrt{\frac{\sum_{I=1}^{N} (\tau_I - \tau_I^{\text{exact}})^2}{N}}, \tag{35}$$

$$L_\infty(\tau_I) = \max_{I \in N} (\tau_I - \tau_I^{\text{exact}}), \tag{36}$$

and comparing the results in Tables 2 and 3, it is evident that the errors in ϕ from RDF generation preclude convergence at the local level, although the spatially-averaged results retain acceptable accuracy. The localized surface smoothing in some instances can reduce errors by nearly 50%.

In the second mesh sweep, the use of Eq. (29) to generate estimates of $\tau_{I'}$ represents a second application of surface smoothing that involves more surrounding interface markers. To understand the effect of errors in τ_I estimation on the near-interface turbulence treatment, we introduce the following error measures on y^+_{Int} and $f_{\mu\text{Int}}$:

$$L_2(y^+_{\text{Int}}) = \sqrt{\frac{1}{V} \int_V \left(\frac{y^+_{\text{Int}} - y^{+\text{exact}}_{\text{Int}}}{y^{+\text{exact}}_{\text{Int}}} \right)^2 \mathrm{d}V}, \tag{37}$$

$$L_\infty(y^+_{\text{Int}}) = \max_{\in V} \left(\frac{y^+_{\text{Int}} - y^{+\text{exact}}_{\text{Int}}}{y^{+\text{exact}}_{\text{Int}}} \right), \tag{38}$$

$$L_2(f_{\mu\text{Int}}) = \sqrt{\frac{1}{V} \int_V (f_{\mu\text{Int}} - f^{\text{exact}}_{\mu\text{Int}})^2 \, \mathrm{d}V}, \tag{39}$$

$$L_\infty(f_{\mu\text{Int}}) = \max_{\in V} (f_{\mu\text{Int}} - f^{\text{exact}}_{\mu\text{Int}}). \tag{40}$$

Table 2
Spatial averages and errors on interfacial shear stress τ_I for the problem of tangential annular flow, in the case of the analytical solution for the distance function of the annular cross-section being imposed

Mesh	τ_I without surface smoothing			τ_I after surface smoothing		
	$\langle\tau_I\rangle/\tau_I^{\text{exact}}$	$L_2(\tau_I)$	$L_\infty(\tau_I)$	$\langle\tau_I\rangle/\tau_I^{\text{exact}}$	$L_2(\tau_I)$	$L_\infty(\tau_I)$
Concave interface						
$32 \times 32 \times 4$	0.92696	9.42×10^{-2}	1.56×10^{-1}	0.97176	3.27×10^{-2}	6.24×10^{-2}
$64 \times 64 \times 8$	0.97699	3.25×10^{-2}	8.32×10^{-2}	0.99272	8.19×10^{-3}	1.10×10^{-2}
$128 \times 128 \times 16$	0.99416	9.39×10^{-3}	2.44×10^{-2}	0.99366	8.46×10^{-3}	1.78×10^{-2}
Convex interface						
$32 \times 32 \times 4$	1.02230	2.66×10^{-2}	5.02×10^{-2}	1.01537	1.61×10^{-2}	2.17×10^{-2}
$64 \times 64 \times 8$	1.01306	1.75×10^{-2}	4.04×10^{-2}	1.00733	8.62×10^{-3}	2.07×10^{-2}
$128 \times 128 \times 16$	1.00492	6.40×10^{-3}	1.46×10^{-2}	1.00267	3.08×10^{-3}	6.36×10^{-3}

Table 3
Spatial averages and errors on interfacial shear stress τ_I for the problem of tangential annular flow

Mesh	τ_I without surface smoothing			τ_I after surface smoothing		
	$\langle\tau_I\rangle/\tau_I^{\text{exact}}$	$L_2(\tau_I)$	$L_\infty(\tau_I)$	$\langle\tau_I\rangle/\tau_I^{\text{exact}}$	$L_2(\tau_I)$	$L_\infty(\tau_I)$
Concave interface						
$32 \times 32 \times 4$	0.94993	9.52×10^{-2}	1.59×10^{-1}	0.95994	8.53×10^{-2}	1.41×10^{-1}
$64 \times 64 \times 8$	0.93685	1.28×10^{-1}	3.28×10^{-1}	0.97269	6.18×10^{-2}	1.29×10^{-1}
$128 \times 128 \times 16$	0.97048	1.41×10^{-1}	4.92×10^{-1}	0.95745	6.05×10^{-2}	1.66×10^{-1}
Convex interface						
$32 \times 32 \times 4$	1.06582	1.14×10^{-1}	2.25×10^{-1}	1.03291	6.20×10^{-2}	1.10×10^{-1}
$64 \times 64 \times 8$	1.00320	8.68×10^{-2}	3.18×10^{-1}	1.00021	3.45×10^{-2}	1.19×10^{-1}
$128 \times 128 \times 16$	0.98569	9.20×10^{-2}	2.46×10^{-1}	0.97230	4.67×10^{-2}	1.26×10^{-1}

The distance function at cell-center locations was reconstructed from CVTNA interface reconstructions on the twice-as-fine VOF mesh and using tautening in the vicinity of the zero level, and cell-edge estimates subsequently obtained using arithmetic averaging.

Table 4 shows the results obtained using the exact distance function to be strongly convergent, with second-order accuracy achievable for both y^{+}_{Int} and $f_{\mu\mathsf{Int}}$. The left half of Fig. 9 highlights the ability of the new near-

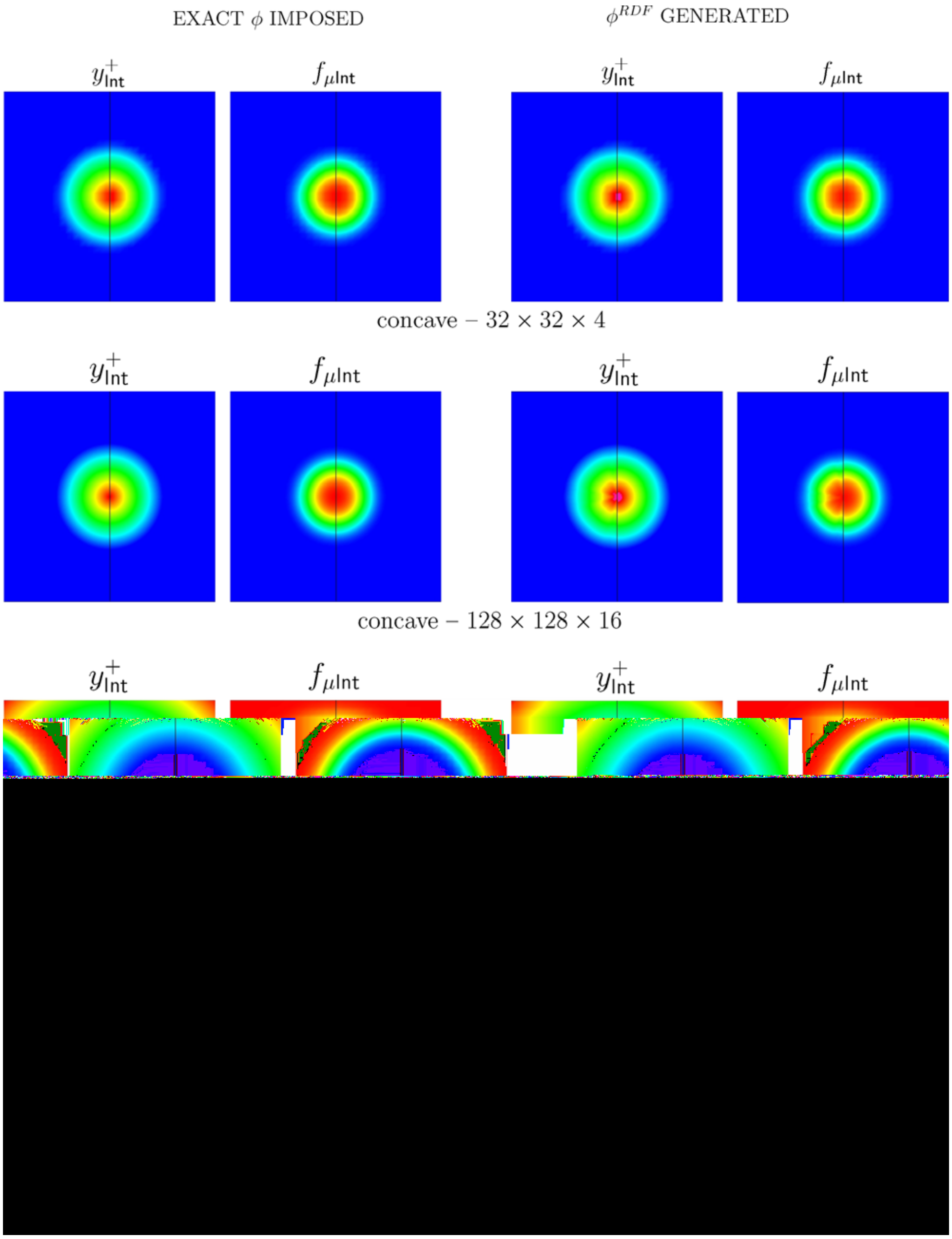

Fig. 9. Distributions of y^+_{Int} and $f_{\mu\mathsf{Int}}$ computed for the problem of tangential annular flow, for the cases of the analytical solution for the distance function ϕ being imposed (left half of figure), and for the case of ϕ being reconstructed (CVTNA, twice-as-fine VOF mesh, tautening procedure) with subsequent arithmetic averaging for cell-edge estimates. In each panel, the left side of the black line represents the results of y^+_{Int} and $f_{\mu\mathsf{Int}}$ generated by the RISV algorithm, while the right side represents the analytical solutions to y^+_{Int} and $f_{\mu\mathsf{Int}}$.

available in the companion paper [5]. Overall, introducing the near-interface treatment via Eq. (20) has been found to considerably enhance the quality of the results as compared to the Smagorinsky model alone.

6. LES of wave breaking

Wave breaking in coastal engineering research has traditionally been treated as a free surface flow, using single-fluid hydro-codes based on free surface models imposing zero pressure boundary conditions, e.g.

Table 5
Errors on the near-interface non-dimensional length scale, y^+_{Int}, and the near-interface turbulence damping factor, $f_{\mu\mathrm{Int}}$, for the problem of tangential annular flow

Mesh	$L_2(y^+_{\mathrm{Int}})$	$L_\infty(y^+_{\mathrm{Int}})$	$L_2(f_{\mu\mathrm{Int}})$	$L_\infty(f_{\mu\mathrm{Int}})$
Concave interface				
$32 \times 32 \times 4$	7.74×10^{-2}	3.49×10^{-1}	1.57×10^{-2}	4.18×10^{-2}
$64 \times 64 \times 8$	6.25×10^{-2}	4.74×10^{-1}	2.23×10^{-2}	6.43×10^{-2}
$128 \times 128 \times 16$	1.97×10^{-1}	3.88	2.16×10^{-2}	7.39×10^{-2}
Convex interface				
$32 \times 32 \times 4$	4.50×10^{-2}	1.21×10^{-1}	1.92×10^{-2}	5.35×10^{-2}
$64 \times 64 \times 8$	3.97×10^{-2}	4.57×10^{-1}	1.38×10^{-2}	5.93×10^{-2}
$128 \times 128 \times 16$	2.97×10^{-2}	3.18×10^{-1}	1.45×10^{-2}	5.51×10^{-2}

The distance function at cell-center locations were reconstructed from CVTNA interface reconstructions on the twice-as-fine VOF mesh and using tautening in the vicinity of the zero level, and cell-edge estimates subsequently obtained using arithmetic averaging.

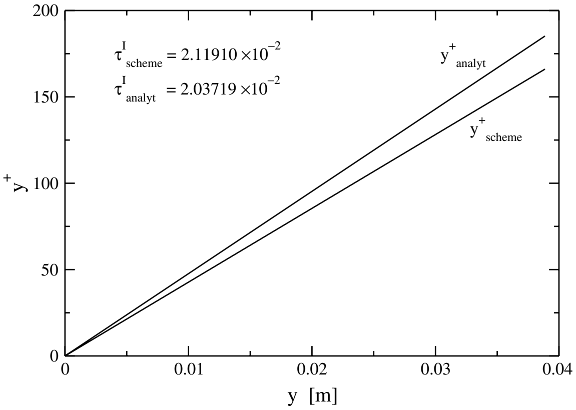

Fig. 10. Analytical and computed non-dimensional length scales for the turbulence to the gas side of the deformable interface, for the $Re^* = 171$ case of Fulgosi et al.

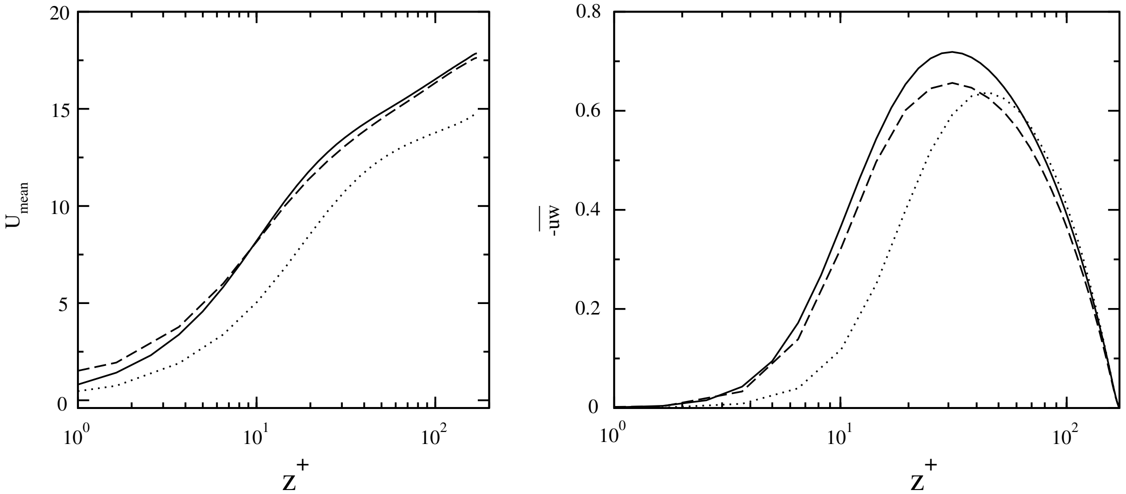

Fig. 11. Comparison of mean velocity and shear stress profiles in wall coordinates: (—), DNS; (–––), LES with SGS and Eq. (20); (···), LES with SGS alone.

[29,30]. Such treatments, on their own, provide no insight into the air flows above the free surface, and the effect of such air flows on water wave motions. Given the dependence of wave height and steepness on wind speed [31], non-uniform distributions of form drag to the gas-side of propagating and breaking waves [32], and significant populations of coherent structures either side of sheared interface [6], it is desirable that flow models of wave breaking capture the details of turbulence either side of the free surface. The use of multi-fluid CFD codes based on numerical schemes that sharply capture shear at the free surface, in the manner of the schemes presented in this paper, should represent a tangible improvement in predictive capability. Using such codes, local gas-sided wind-induced effects and turbulent wave-induced mixing should be realistically captured in the vicinity of the free surface. In marine climatology, studies of CO_2 absorption by the oceans using multi-fluid CFD codes should correctly represent interphase mass transfer rates, covering plunging, breaking and micro-breaking flow conditions. Since these flows are beyond the capability of DNS (in the strict sense of turbulence), the LES approach is the only viable alternative for similar environmental problems. The proper use of LES for such problems requires near-interface multi-physics modelling support, in the form of DNS-based turbulence modification in SGS models and mass transfer correlations.

6.1. Model setup and flow initialization

For this work, a constant bed slope is assumed, and simulation using a Cartesian mesh and off-vertical gravity contributions is ideal; Fig. 12 shows the setup of the computational mesh. Solution domain dimensions are chosen to achieve some similarity with the problem initialization used by Christensen and Deigaard [29]. In the present, the streamwise breadth of $X = 8.0$ m is resolved by $nx = 200$ cells, the vertical direction of breadth of $Z = 0.6$ m is resolved by $nz = 80$ cells, the spanwise breadth of $Y = 0.3$ m is resolved by 40 cells, and the bed angle β is 4.23°. A preliminary coarse-grid resolution of $140 \times 40 \times 20$ was not sufficient to resolve the interface viscous sublayers, and as such the details of the interface wrinkling were smoothed out. The fine grid resolution helped resolve the viscous sublayers at both the wall (channel bed) and the gas-side interface down to $y^+_{\mathrm{Wall}} \approx y^+_{\mathrm{Int}} \approx 0.5$, with occasionally lower local (spot) values at the interface (≈ 0.1). The subsequent discussion focuses on the fine grid resolution results.

The fifth-order Stokes theory solution derived by Fenton [33] is the basis of the free surface and boundary conditions initialization used here. To compute the appropriate free surface and boundary conditions according to this theory, it is necessary to specify the mean bath depth d, the wave amplitude H, the wave period T, the Stokes drift velocity c_S, and gravity g. For the current study, we choose parameter values that share some similarity with the parameters used by Christensen and Deigaard [29] in their "weak plunger" case, although in our case the wave amplitude is higher. Specifically, we set $d = 0.321$ m, $H = 0.12$ m, $T = 1.4$ s, $c_S = 0$ m/s, and $g = 9.81$ m/s^2. Because of the tilt of the computational domain, the origin used to initialize the free surface wave is shifted to the left distance $h/\mathrm{cotan}(\beta)$, and represents the origin of an unrotated coordinate space specifically for free surface initialization. The offshore boundary is prescribed as a fixed boundary condition, with the velocities computed as partial derivatives of the velocity potential determined according to [33]; this results in a periodic behaviour in the inflows and outflows of water from the computational domain. The scaling procedure proposed by Christensen and Deigaard [29] is used to ensure the total flux at the offshore boundary does not deviate from the theory, even in the presence of surface level fluctuations at the offshore boundary. The velocity distribution of the air entering the solution domain at the offshore boundary is initialized to share the velocity of the water at the free surface level, to minimize shear at the interface/offshore-boundary

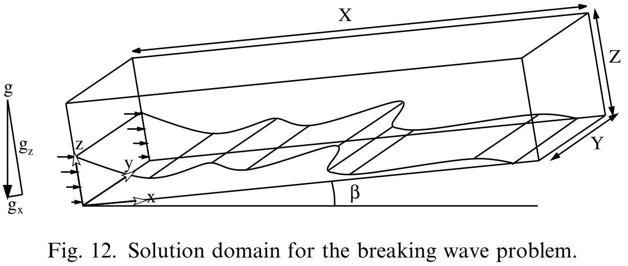

Fig. 12. Solution domain for the breaking wave problem.

junction. The on-shore boundary is treated as an open boundary condition, the bed is represented using no-slip boundary conditions, with a low-*Re* number resolution that avoids resorting to wall functions. The eddy viscosity is employed in the form of Eq. (19) too, albeit with the original van Driest damping function for wall-bounded flows. The upper plane is treated as a free-slip boundary, whereas the lateral ones are represented as periodic boundaries.

Unlike in pressure-gradient driven flows (channels or boundary layers), the setup in this case requires the flow to be initially at rest; the flow – including the surface deformations – then starts to develop under the action of gravity. A rough estimate of the Reynolds number based on the mean depth d of the 'potential' liquid flow is about $Re_d^{\mathrm{pot}} = 140$. Once the potential energy of the liquid is transformed into kinetic energy, the actual Reynolds number should be way smaller compared to Re_d^{pot} with time. The fluctuating turbulent field initially imposed was generated using a Gaussian distribution with zero mean and a standard deviation of $\sigma_u = 0.1\sqrt{gd\sin(\beta)}$. After steady-state solutions were obtained (six seconds of real time), the shear-based Reynolds number was found to converge in both phases towards $Re^* = U_\tau d/\nu \approx 400$.

6.2. Simulation results

6.2.1. Macroscale flow assessment

Mesh dependence studies were carried out using progressively coarser meshes ($200 \times 40 \times 80$, $100 \times 20 \times 40$, $50 \times 10 \times 20$). Fig. 13 shows the time history of free surface elevation extracted at six equally spaced locations along the mean free surface profile; the upper gray line denotes the mean profile, while the lower gray line identifies the bed depth for the relevant x-coordinate. The profiles show the free surface evolution to feature variable degrees of periodicity, with the more offshore locations showing sustained periodicity, resembling the Stokes-theory flux boundary condition if prescribed there, and the near-shore locations ahead of the wave plunging exhibiting substantial irregularity in crest elevations and frequencies. The flow also tends towards ergodic rather quickly after the start-up phase (the first wave period), which is characterized by a higher-amplitude first crest and trough emanating from the offshore boundary. The noise occasionally observed corresponds to free surface underneath and preceding the propagating steep wave crest tending towards vertical and shooting out ahead of the crest.

The uppermost plots in Fig. 13, corresponding to the more offshore locations, show the crests and trough for the low-resolution simulations to be out of phase by $\sim 0.33T$, as compared to the high-resolution results. Most of this phase error was induced in start-up, and the action of the Stokes-theory offshore boundary wave-sustainer ensures the propagation velocity of the subsequent waves is much more accurate, with period errors by about $0.05T$ only. In the crests and troughs for the more offshore locations, crest heights and trough depths from the different meshes can vary by up to $0.25H$ between successive meshes, but the heights and depths are not systematically under- or overestimated. These results are a first indicator confirming the macroscopic features of the statistically steady-state flow to be adequately resolved.

Closer to the shore, the free surface elevation history remains strongly periodic, albeit taking longer for ergodicity to sustain. The lower-resolution histories are far less regular, and suggest that the wave-breaking events can be better resolved in the vicinity of the shore zones.

A common comparison with experiment made in wave breaking is the ratio of wave height to bath depth, $\gamma_{\mathrm{b}} \equiv H_{\mathrm{b}}/d_{\mathrm{b}}$, commonly referred to as the breaker index. Wave height H_{b} is measured as the vertical distance between the crest and the adjacent trough at breaking, while bath depth d_{b} is based on the quiescent bath level. For plane slope beds, Smith and Kraus [34] generated the following best-fit linear relation for the breaker index as a function of bed slope and wave steepness:

$$\gamma_{\mathrm{b}} = \frac{H_{\mathrm{b}}}{d_{\mathrm{b}}} = b(m) - a(m)\left(\frac{H_0}{L_0}\right), \tag{41}$$

where $a(m) = 5.00(1 - \mathrm{e}^{-43m})$ and $b(m) = 1.12/(1 + \mathrm{e}^{-60m})$. Eq. (41) was derived from multiple data sets, for data ranges of $0.0007 \geqslant H_0/L_0 \geqslant 0.0921$, and $1/80 \geqslant m \geqslant 1/10$. Upon fully-developed flow being established, the breaking point for waves in the simulation break is in the vicinity of $x = 1.95m \pm 0.10m$, and $\gamma_{\mathrm{b}}^{\mathrm{simulation}} \approx 0.82$. Given the deep wave steepness and bed slope for the current setup, Eq. (41) yields

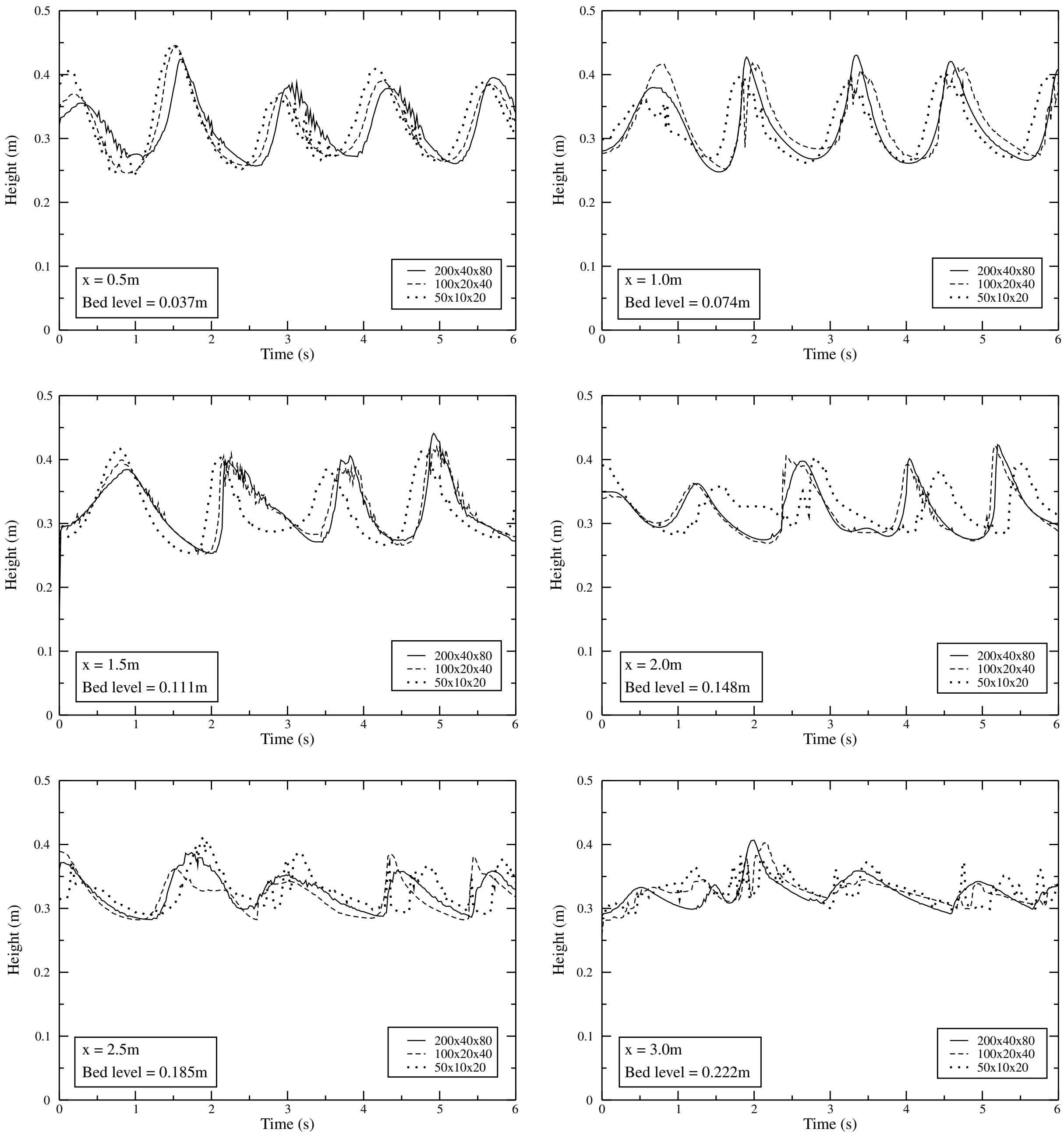

Fig. 13. Time history and mesh dependence of surface elevation at difference horizontal locations in the flow domain.

$\gamma_{\mathrm{b}}^{\mathrm{experiment}} \approx 0.85$. The measured breaker index from the simulation is within the error associated with the scatter of the experimental data, and is a validation of the macro-scale representation of the flow. Compared with the weak plunger result in [29] of 0.95–1.0, our case features a lower value of γ_{b} because the substantially higher wave height results in the propagating waves “feeling bottom” further offshore. Even with the differences in wave height, longshore-averaged velocity profiles from the simulation share significant qualitative resemblance with the simulation results of Christensen and Deigaard [29], as well as with the experimental data of Ting and Kirby [35].

6.2.2. Wave breaking events

Although the problem setup corresponds (for the most part) to the “weak plunger” breaker type in [29], flow scenarios resembling the spilling and plunging breaker types have also been observed. In the spilling event captured in the simulation, the wave rolls through the crest without any liquid being thrown ahead of the crest. In the weaker plunging event – which is dominant in this simulation – a tongue of water is thrown forward of the crest, before impacting with the free surface in front of the crest. In the stronger plunging event, the tongue is thrown much further ahead of the crest. Rather than the plunger fully rebounding off the free surface, air entrainment is seen indicating penetration of the plunger, and there is an upward rise of liquid in front of the plunger after impact.

Fig. 14 shows the case of a stronger plunging event. The $t = 2.40$ s frame shows the jet having shot ahead of the crest to entrain air under the free surface, which in turn is dragged below the free surface and behind the wave break under the action of the co- and counter-rotative vortices noted by Lubin et al. [36] for plunging waves. The $t = 2.40$ s frame shows the wave propagation to be essentially 2D up to this stage. The thinning of the jet ejected forward from the crest coincides with the onset of interface wrinkles in the jet that are perpendicular to the long-shore spanwise direction – this represents the first visible signs of three-dimensionality in

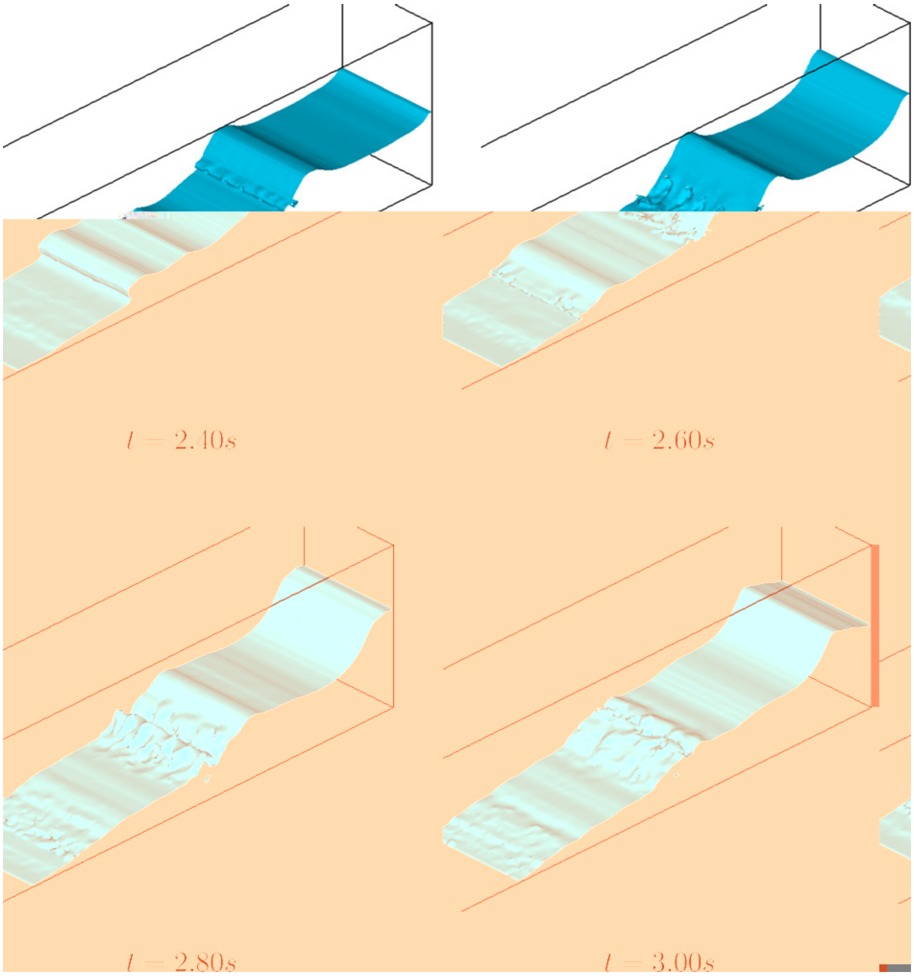

Fig. 14. 3D views of $C = 0.5$ isosurface frames during the same stronger plunging event, showing the interface wrinkling induced perpendicular to the spanwise direction. This substantial three dimensionality in free surface deformations occurs exclusively during the wave breaking, and the free surface regains smoothness soon after.

free surface deformation. At this point, the flow diverges from the scenario of Lubin et al. [36], which, by setup, is largely laminar and 2D in nature.

The $t = 2.60$ s frame shows the jet impacting with the free surface ahead of the wave to have filamented, and the leading surface of the breaker to be deformed in a 3D manner by the wrinkling perpendicular to the spanwise direction: at this time, up to five dominant long-wavelength wrinkles are apparent in the free surface ahead of the crest at the base of the wave lip.

At $t = 2.80$ s, each of the long-wavelength wrinkles perpendicular to the spanwise direction are divided into two. The free surface of the wave behind the impact area is falling, and one set of the wrinkles appear on its leading surface. The upward rise of liquid in front of the impact features the section of the free surface corresponding to the leading edge of the wave lip from the previous frame. The liquid just ahead of the wave break impact area features wrinkles of the same long-wavelength mode even after penetration of the breaking wave below the impacted free surface, but are of higher amplitude, i.e. deeper.

In the last frame of Fig. 14 at $t = 3.00$ s, the long-wavelength interface wrinkles on the wave behind the impact area propagate up the leading surface and over the crest, and amplify in magnitude. In contrast, the previously higher-amplitude interface wrinkles ahead of the impact zone have dissipated, and the three-dimensionality of the interface has been replaced by a substantial regaining of the free surface's smoothness and two-dimensional character during normal wave propagation. As seen from the free surface between the impact zone and the shore, the 3D interface wrinkles induced by the breaking are smoothed out completely, thus restoring the two-dimensionality of the free surface.

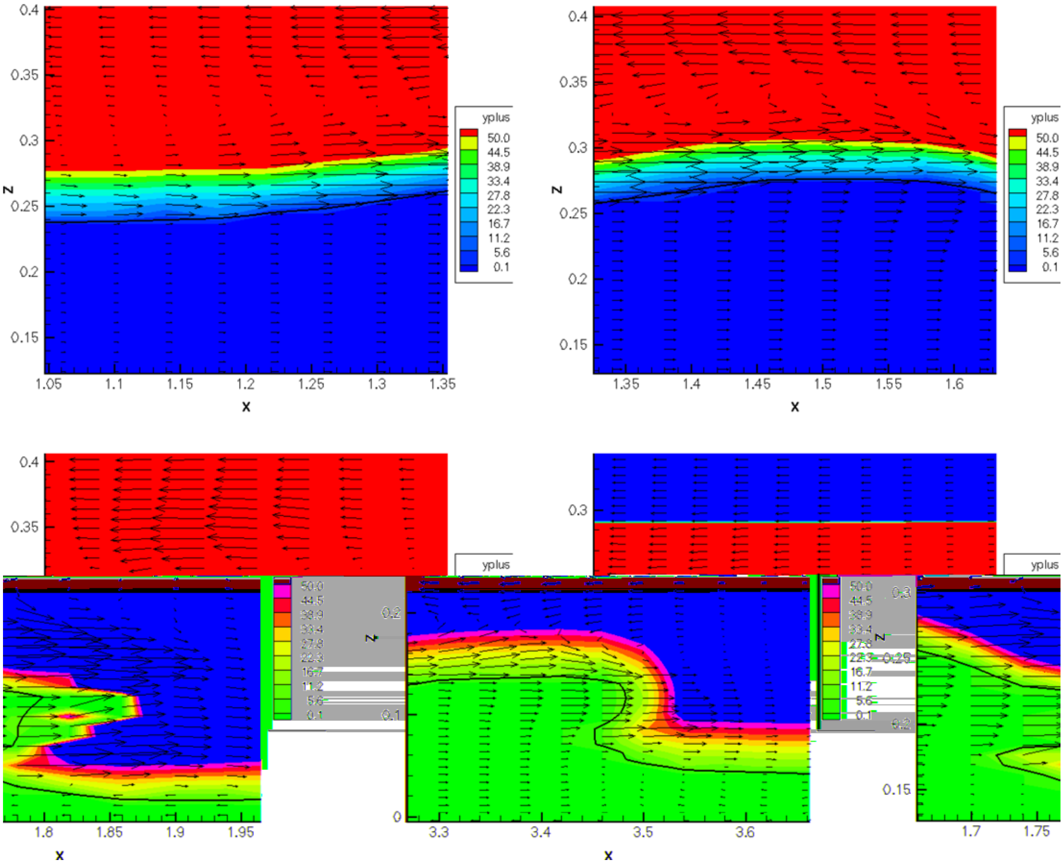

Fig. 15. Resolved interfacial sublayer colored by "interface turbulence units" contours.

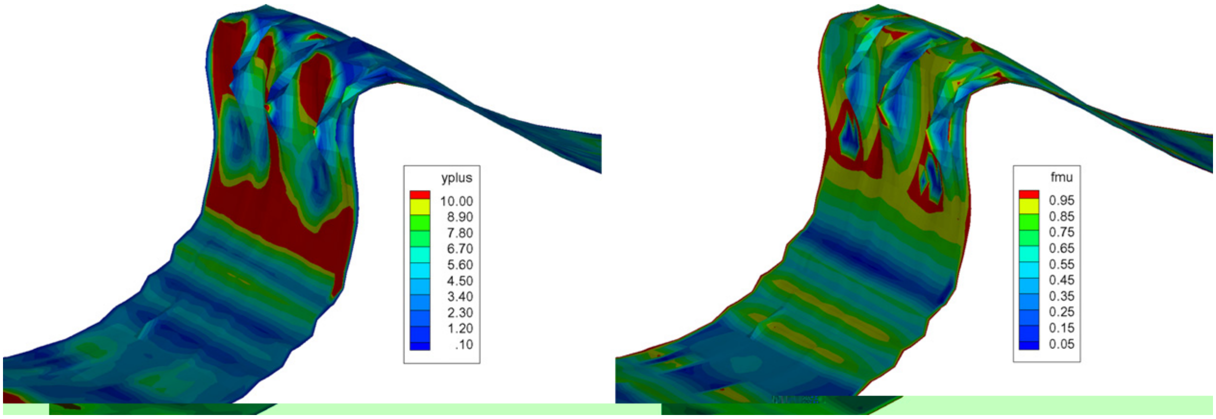

Fig. 16. Interfacial contours of "interface turbulence units" and corresponding damping function levels (y_{Int}^{+} and $f_{\mu\mathrm{Int}}$) prior to wave breaking ($t = 0.55$ s).

6.2.3. Near-interface sublayer

The near-interface turbulence decay treatment is best illustrated in Fig. 15, displaying various snapshots of the streamwise velocity vector field around the deformable interface, and contours of the interface turbulence unit y_{Int}^{+}. It is clearly shown that the interfacial resolution is of the order of $y_{\mathrm{Int}}^{+} = 0.2$–$0.4$, which is the prerequisite for a pure low-*Re* number resolution that dispenses with the use of wall functions. The interfacial shear is clearly well captured, without being smeared. Independent of the shape of the interface, the approach presented in this paper for near-interface treatment is capable of providing a well defined interfacial viscosity-affected support, and provides a foundation for numerous other near-interface multi-physics treatment.

The interfacial contour levels of y_{Int}^{+} and corresponding $f_{\mu\mathrm{Int}}$ are shown in Fig. 16. These data correspond to a specific flow event prior to wave breaking simulated in the previous sequence. The change in the y_{Int}^{+} values and its dependence on the wave deformation is clear from both panels. The y_{Int}^{+} spectrum lies within the range [0.1–10], meaning that the viscosity-affected region is well resolved. We could notice in particular that there are only a couple of zones where the damping function asymptotes towards unity, namely at the downslope region of the wave. In the small-scale surface wrinkling region located around the crest, $f_{\mu\mathrm{Int}}$ values oscillate strongly in response to the undulation of shear induced by the vortical structures nestled between adjacent wrinkles, as it has been discussed in the context of Fig. 14. The RISV scheme realistically captures the shearing action of the vortices nestled between the wrinkles, and results in y_{Int}^{+} scaling rapidly with the filter scale. Away from the turbulence generation zone corresponding to the impact area of the breaker (trough), the near-interface treatment acts to impose the correct laminarization of the viscous sublayer to the gas-side. Turbulence damping of the form shown in the trough at Fig. 16(left) contributes in particular to the restoring of the correct smoothness of the surface after impact. The smoothness takes time to establish, because of the need for the vortical structures on the liquid side of the free surface to dissipate.

7. Conclusions

A new algorithm for correcting shear-dependent asymptotic behaviour of turbulence at arbitrarily deformable interfaces has been developed, and described in this paper in implementation detail. The application of the algorithm to wave breaking has also been outlined. Detailed information about near-interface turbulent transport in wave breaking has been obtained using the algorithm; a communication of these results is underway.

With the availability of high-quality reconstructed distance function data, the RISV scheme introduced here is able to ensure a correct mapping between the physical distance to the interface and turbulence units length-scale. The key to the utility of the RISV is its basis in gas-sided (or liquid-sided) velocity field extrapolation. Beyond simple interpolation across the interface, the RISV scheme ensures applicability to multi-fluid flows featuring large discontinuities and large gradients either side of any discontinuities; gas-sided estimates of the shear velocity U_τ are not contaminated by quantitatively different liquid-sided velocity gradients, and vice-versa.

For the LES of turbulent interfacial flows, the major source of error in interfacial shear estimation is associated with the determination of the distance function. Specifically, the presence of high-frequency error in the vicinity of the zero level scatters the trajectories traced back from interface-vicinity mesh points to the interface itself. While a localized surface smoothing reduces this noise, the design of the RISV scheme to maintain the sharpness of interfacial shear gradients suggests that further improvements could result from the availability of more accurate and smoother distance function data. The testing in this work shows the error in the RDF to slightly broaden the interface wall units length scale, resulting in a slight overestimation of the near-interface damping prescribed for the Smagorinsky SGS model.

The development of a scheme for RDF generation throughout a non-compact interface support shows our near-interface multi-physics treatment is not necessarily linked to the use of level-set interface tracking. Our approach to RDF generation features a level of simplicity required to reconstruct distance functions from VOF interface reconstruction data in a feasibly efficient manner. Further, the tautening of the RDF about the zero level presented here provides a high degree of smoothness that makes the algorithm useful for interfacial shear estimation. More importantly, the RDF is intimately tied to the VOF representation of the interface, and can be easily implemented. It helps make our near-interface multi-physics modelling capability readily implementable in well-established VOF-based codes.

Acknowledgements

Professor George Yadigaroglu (ETH Zurich) is acknowledged for his support of this work. Dr. Doug Kothe (Los Alamos National Laboratory) is also acknowledged for his valuable comments on this work.

References

[1] P. Liovic, D. Lakehal, J.-L. Liow, LES of turbulent bubble formation and break-up based on interface tracking, in: B.J. Geurts, R. Friedrich, O. Metais (Eds.), Direct and Large-Eddy Simulation V ERCOFTAC Series, vol. 10, Kluwer Academic Publishers, Dordrecht, 2004, pp. 261–270.

[2] P. Liovic, D. Lakehal, Interface–turbulence interactions in large-scale bubbling processes, Int. J. Heat Fluid Flow 27 (2006), doi:10.1016/j.ijheatfluidflow.2006.03.003.

[3] D. Lakehal, DNS and LES of turbulent multifluid flows, in: Proceedings of the 3rd International Symposium of Two-Phase Flow Modelling and Experimentation, Pisa, Italy, September 22–26, 2004.

[4] M. Germano, U. Piomelli, P. Moin, W.H. Cabot, A dynamic subgrid-scale eddy viscosity model, Phys. Fluids 3 (1991) 1760–1765.

[5] D. Lakehal, S. Reboux, P. Liovic, SGS modelling for the LES of interfacial gas–liquid flows, La Houille Blanche – Revue Internationale de L'eau 6 (2005) 125–131.

[6] M. Fulgosi, D. Lakehal, S. Banerjee, V. De Angelis, Direct numerical simulation of turbulence in a sheared air–water flow with a deformable interface, J. Fluid Mech. 482 (2003) 319–345.

[7] S. Osher, J. Sethian, Fronts propagating with curvature-dependent speed: algorithms based on Hamilton–Jacobi formulations, J. Comput. Phys. 79 (1988) 12–49.

[8] J. Glimm, J.W. Grove, X.L. Li, K.M. Shyue, Y.N. Zeng, Q. Zhang, 3-Dimensional front tracking, SIAM J. Sci. Comput. 19 (1998) 703–727.

[9] S.O. Unverdi, G. Tryggvason, A front-tracking method for viscous, incompressible, multi-fluid flows, J. Comput. Phys. 100 (1992) 25–37.

[10] R. Debar, Fundamentals of the KRAKEN code, Technical Report UCIR-760, Lawrence Livermore National Laboratory, 1974.

[11] W.F. Noh, P.R. Woodward, SLIC (simple line interface method), in: A.I. van de Vooren, P.J. Zandbergen (Eds.), Lecture Notes in Physics, vol. 59, 1976, pp. 330–340.

[12] C.W. Hirt, B.D. Nichols, Volume of fluid (VOF) method for the dynamics of free boundaries, J. Comput. Phys. 39 (1981) 205–226.

[13] M. Rudman, A volume-tracking method for incompressible multi-fluid flows with large density variations, Int. J. Numer. Methods Fluids 28 (1998) 357–378.

[14] M. Bussmann, D.B. Kothe, J.M. Sicilian, Modeling high density ratio incompressible interfacial flows, in: Proceedings of ASME Fluids Engineering Division Summer Meeting, Montreal, 14–18 July, 2002, FEDSM2002-31125.

[15] M. Sussman, E.G. Puckett, A coupled level set and volume-of-fluid method for computing 3D and axisymmetric incompressible two-phase flows, J. Comput. Phys. 162 (2000) 301–337.

[16] S.J. Cummins, M.M. Francois, D.B. Kothe, Estimating curvature from volume fractions, Comput. Struct. 83 (2005) 425–434.

[17] P. Liovic, M. Rudman, J.-L. Liow, D. Lakehal, D.B. Kothe, A 3D unsplit-advection volume tracking algorithm with planarity-preserving interface reconstruction, Comp. Fluids 35 (2006) 1011–1032.

[18] D. Lakehal, M. Fulgosi, G. Yadigaroglu, S. Banerjee, Direct numerical simulation of turbulent heat transfer across a mobile, sheared gas–liquid interface, J. Heat Transfer 125 (2003) 1129–1139.
[19] S. Banerjee, D. Lakehal, M. Fulgosi, Surface divergence models for scalar exchange between turbulent streams, Int. J. Multiphase Flow 30 (2004) 963–977.
[20] D. Lakehal, M. Milelli, B.L. Smith, Large-eddy simulation of bubbly turbulent shear flows, J. Turbulence 3 (2002) 1–21.
[21] P. Liovic, J.-L. Liow, M. Rudman, A volume-of-fluid (VOF) method for the simulation of metallurgical flows, ISIJ Int. 41 (2001) 225–233.
[22] D.L. Youngs, Time-dependent multi-material flow with large fluid distortion, in: K.W. Morton (Ed.), Numerical Methods for Fluid Dynamics, 1982, pp. 273–285.
[23] B. Vreman, B. Geurts, H. Kuerten, A priori tests of large eddy simulation of the compressible plane mixing layer, J. Eng. Math. 29 (1995) 299–327.
[24] M.M. Francois, S.J. Cummins, E.D. Dendy, D.B. Kothe, J.M. Sicilian, M.W. Williams, A balanced-force algorithm for continuous and sharp interfacial surface tension models within a volume tracking framework, J. Comput. Phys. 213 (2006) 141–173.
[25] D.L. Chopp, Computing minimal surfaces via level set curvature flow, J. Comput. Phys. 106 (1993) 77–91.
[26] M. Sussman, P. Smereka, S. Osher, A level set approach for computing solutions to incompressible two-phase flow, J. Comput. Phys. 114 (1994) 146–159.
[27] J.A. Sethian, P. Smereka, Level set methods for fluid interfaces, Annu. Rev. Fluid Mech. 35 (2003) 341–372.
[28] R.B. Bird, W.E. Stewart, E.N. Lightfoot, Transport Phenomena, Wiley, New York, 1960.
[29] E.D. Christensen, R. Deigaard, Large eddy simulation of breaking waves, Coastal Eng. 42 (2001) 53–86.
[30] Q. Zhao, S. Armfield, K. Tanimoto, Numerical simulation of breaking waves by a multi-scale turbulence model, Coastal Eng. 51 (2004) 53–80.
[31] A.D. Jenkins, Do strong winds blow waves flat? in: B.L. Edge, J.M. Hemsley (Eds.), Proceedings WAVES 2001, Ocean Wave Measurement and Analysis, vol. 1, American Society of Civil Engineers, 2002, pp. 494–501.
[32] D. Lakehal, P. Liovic, Large eddy simulation of steep water waves, in: S. Balachandar, A. Prosperetti (Eds.), IUTAM Symposium on Computational Approaches to Multiphase Flow, Fluid Mechanics and its Applications Series, vol. 81, Springer, 2006, pp. 331–340.
[33] J.D. Fenton, A fifth-order Stokes theory for steady waves, J. Waterw. Port Coastal Ocean Eng. 111 (1985) 216–234.
[34] E. Smith, N.C. Kraus, Laboratory study of wave-breaking over bars and artificial reefs, J. Waterw. Port Coastal Ocean Eng. 117 (1991) 307–325.
[35] F.C.K. Ting, J.T. Kirby, Observations of undertow and turbulence in a laboratory surf zone, Coastal Eng. 24 (1994) 51–80.
[36] P. Lubin, S. Vincent, J.-P. Caltagirone, S. Abadie, Fully three-dimensional direct numerical simulation of a plunging breaker, C. R. Mecanique 331 (2003) 495–501.